



Aberystwyth University

Aerodynamic roughness of glacial ice surfaces derived from high-resolution topographic data

Smith, Mark W.; Quincey, Duncan Joseph; Dixon, Timothy; Bingham, Robert G.; Carrivick, Jonathan L.; Irvine-Fynn, Tristram; Rippin, David M.

Published in:

Journal of Geophysical Research: Earth Surface

DOI:

[10.1002/2015JF003759](https://doi.org/10.1002/2015JF003759)

Publication date:

2016

Citation for published version (APA):

Smith, M. W., Quincey, D. J., Dixon, T., Bingham, R. G., Carrivick, J. L., Irvine-Fynn, T., & Rippin, D. M. (2016). Aerodynamic roughness of glacial ice surfaces derived from high-resolution topographic data. *Journal of Geophysical Research: Earth Surface*, 121(4), 748-766. <https://doi.org/10.1002/2015JF003759>

General rights

Copyright and moral rights for the publications made accessible in the Aberystwyth Research Portal (the Institutional Repository) are retained by the authors and/or other copyright owners and it is a condition of accessing publications that users recognise and abide by the legal requirements associated with these rights.

- Users may download and print one copy of any publication from the Aberystwyth Research Portal for the purpose of private study or research.
- You may not further distribute the material or use it for any profit-making activity or commercial gain
- You may freely distribute the URL identifying the publication in the Aberystwyth Research Portal

Take down policy

If you believe that this document breaches copyright please contact us providing details, and we will remove access to the work immediately and investigate your claim.

tel: +44 1970 62 2400
email: is@aber.ac.uk

Aberystwyth University

Aerodynamic roughness of glacial ice surfaces derived from high-resolution topographic data

Smith, Mark W.; Quincey, Duncan Joseph; Dixon, Timothy; Bingham, Robert G.; Carrivick, Jonathan L.; Irvine-Fynn, Tristram; Rippin, David M.

Published in:

Journal of Geophysical Research: Earth Surface

DOI:

[10.1002/2015JF003759](https://doi.org/10.1002/2015JF003759)

Publication date:

2016

Citation for published version (APA):

Smith, M. W., Quincey, D. J., Dixon, T., Bingham, R. G., Carrivick, J. L., Irvine-Fynn, T., & Rippin, D. M. (2016). Aerodynamic roughness of glacial ice surfaces derived from high-resolution topographic data. *Journal of Geophysical Research: Earth Surface*, 121. 10.1002/2015JF003759

General rights

Copyright and moral rights for the publications made accessible in Cadair (the Institutional Repository) are retained by the authors and/or other copyright owners and it is a condition of accessing publications that users recognise and abide by the legal requirements associated with these rights.

- Users may download and print one copy of any publication from Cadair for the purpose of private study or research.
- You may not further distribute the material or use it for any profit-making activity or commercial gain
- You may freely distribute the URL identifying the publication in Cadair

Take down policy

If you believe that this document breaches copyright please contact us providing details, and we will remove access to the work immediately and investigate your claim.

tel: +44 1970 62 2400

email: is@aber.ac.uk

Download date: 18. May. 2016

Aerodynamic roughness of glacial ice surfaces derived from high resolution topographic data

Mark W. Smith¹, Duncan J. Quincey¹, Timothy Dixon², Robert G. Bingham³, Jonathan L. Carrivick¹, Tristram D. L. Irvine-Fynn⁴, and David M. Rippin⁵

¹ School of Geography and water@leeds, University of Leeds, Leeds, UK, LS2 9JT

² School of Earth and Environment, University of Leeds, Leeds, UK, LS2 9JT

³ School of GeoSciences, University of Edinburgh, Drummond Street, Edinburgh, UK, EH8 9XP

⁴ Centre for Glaciology, Department for Geography and Earth Sciences, Aberystwyth University, Aberystwyth, UK, SY23 3DB

⁵ Environment Department, University of York, Heslington, York, UK, YO10 5DD

Corresponding author: M. W. Smith, School of Geography and water@leeds, University of Leeds, Leeds, UK, LS2 9JT. (m.w.smith@leeds.ac.uk)

Key Points

- High resolution topographic data permit better glacier ice aerodynamic roughness (z_0) estimates
- Spatial z_0 variability over three orders of magnitude with different temporal trajectories
- Glacier topographic roughness used to upscale z_0 measurements for distributed ablation modeling

Abstract

This paper presents new methods of estimating the aerodynamic roughness (z_0) of glacier ice directly from three-dimensional point clouds and Digital Elevation Models (DEMs), examines temporal variability of z_0 , and presents the first fully distributed map of z_0 estimates across the ablation zone of

27 an Arctic glacier. The aerodynamic roughness of glacier ice surfaces is an important component of
28 energy balance models and meltwater runoff estimates through its influence on turbulent fluxes of
29 latent and sensible heat. In a warming climate these fluxes are predicted to become more significant
30 in contributing to overall melt volumes. Ice z_0 is commonly estimated from measurements of ice
31 surface microtopography, typically from topographic profiles taken perpendicular to the prevailing
32 wind direction. Recent advances in surveying permit rapid acquisition of high resolution topographic
33 data allowing revision of assumptions underlying conventional z_0 measurement. Using Structure from
34 Motion (SfM) photogrammetry with Multi-View Stereo (MVS) to survey ice surfaces with
35 millimeter-scale accuracy, z_0 variation over three orders of magnitude was observed. Different
36 surface-types demonstrated different temporal trajectories in z_0 through three days of intense melt. A
37 glacier-scale 2 m resolution DEM was obtained through Terrestrial Laser Scanning (TLS) and sub-
38 grid roughness was significantly related to plot-scale z_0 . Thus, we show for the first time that glacier-
39 scale TLS or SfM-MVS surveys can characterize z_0 variability over a glacier surface potentially
40 leading to distributed representations of z_0 in surface energy balance models.

41

42 **Index Terms**

43 0738 Ice; 1814 Energy budgets; 1855 Remote sensing; 1863 Snow and ice; 1894 Instruments and
44 techniques: modeling.

45

46 **Keywords**

47 aerodynamic roughness; ice surface energy balance; high resolution topography; anisotropy;
48 Structure from Motion (SfM); Terrestrial Laser Scanning (TLS)

49

50 **1. Introduction**

51

52 In glacier surface energy balance models, turbulent fluxes of sensible and latent heat are generally
53 considered to be secondary to radiative heat fluxes [Hock, 2005]. However, they become increasingly
54 influential (up to 80%) in overcast and windy conditions [Holmgren, 1971; Marcus *et al.*, 1984;
55 Giesen *et al.*, 2014] and for glacierised regions characterized by maritime climates [Hay and
56 Fitzharris, 1988; Ishikawa *et al.*, 1992]. Critically, their relative contribution to overall ice surface
57 mass loss is predicted to become more significant in a warming climate [Braithwaite and Olesen,
58 1990], making it imperative that the key influences on turbulent fluxes are better understood. One of
59 the most important of these influences is the aerodynamic roughness height z_0 , which is related to
60 ice-surface topographic roughness, in a complex way. Improved characterisation of z_0 on glacier ice
61 surfaces forms the focus of this paper.

62
63 All ice-melt models which aim explicitly to incorporate turbulent fluxes, in some way incorporate a
64 value, or range of values, for aerodynamic roughness height, z_0 . This is because, in the absence of
65 direct eddy correlation measurements (which are difficult to obtain in the field; Greuell and Genthon,
66 [2004]), aerodynamic roughness height underpins the derivation of exchange coefficients for
67 potential temperature and specific humidity in the surface boundary layer. These coefficients are
68 often used to approximate turbulent fluxes using the bulk aerodynamic method [Hock, 2005; Brock
69 *et al.*, 2010]. However, z_0 is difficult to measure directly and a range of different approximations are
70 used. For example, spatially distributed surface energy balance models assume a uniform and
71 constant value of z_0 [Arnold *et al.*, 2006] and z_0 is also used as an optimized parameter in the fitting
72 of model output to observations of glacier melt [Hock and Holmgren, 2005].

73
74 Uncertainty in z_0 values presents a serious challenge in the calculation of ice ablation with an order
75 of magnitude change in z_0 leading to a factor of two change in estimated turbulent fluxes [Munro,
76 1989; Hock and Holmgren, 1996; Brock *et al.*, 2010]. Yet field studies have highlighted the
77 variability of z_0 over ice surfaces in both space and time. Brock *et al.* [2006] summarize z_0 values for

78 ice in the published literature, from 0.007 mm for Antarctic blue ice [*Bintanja and van den Broeke*,
79 1994, 1995] to 80 mm for very rough glacier ice [*Smeets et al.*, 1999]. While values over smooth ice
80 are ~ 0.1 mm, the majority of glacier ice z_0 values are in the range of 1–5 mm [*Brock et al.*, 2006].
81 Ablation zones of glaciers can exhibit a large range of ice surface roughness features; however,
82 attempts to model variations in z_0 over single valley glaciers to inform upscaling have proven
83 unsuccessful [*Brock et al.*, 2006]. Considering temporal variability of z_0 , systematic increases in z_0
84 through the ablation season are observed on snow surfaces [*Arnold and Rees*, 2003; *Brock et al.*,
85 2006; *Fassnacht et al.*, 2009b]. However, such systematic increase is less pronounced on glacier ice
86 which exhibits greater temporal variability in z_0 [*Müller and Keeler*, 1969; *Smeets et al.*, 1999; *Denby*
87 *and Smeets*, 2000; *Greuell and Smeets*, 2001; *Brock et al.*, 2006; *Smeets and van den Broeke*, 2008].
88 Such temporal variability remains poorly quantified or constrained.

89

90 The calculation of z_0 from ice surface topography has retained assumptions put in place under
91 conditions of limited topographic data and computational power. The aim of this paper is to address
92 this shortcoming through application of recent advances in high resolution surveying to estimate z_0
93 from ice surface topography. Specifically, we aim to:

94 [1] describe novel parameterizations of surface roughness to represent z_0 that utilize greater
95 availability of high resolution survey data;

96 [2] examine the spatial variability of ice z_0 over the ablation zone of a small Arctic glacier using
97 Structure from Motion;

98 [3] investigate the possibility of upscaling microtopographic z_0 measurements to the glacier
99 scale using Terrestrial Laser Scanning; and

100 [4] characterize the temporal variability of z_0 as ice melt takes place over several days.

101

102 **2. Meaning and measurement of z_0**

103

104 Aerodynamic roughness height, z_0 , is defined herein as a length scale that characterizes the loss of
105 wind momentum attributable to surface roughness [Chappell and Heritage, 2007]; i.e. the height
106 above the ground surface at which the extrapolated horizontal wind velocity drops to zero. The term
107 arises as a constant of integration from the fitting of logarithmic profiles to velocity data as specified
108 by boundary layer theory [Prandtl, 1926; Millikan, 1938] and is estimated for both water and air
109 flows over a wide range of surface types [Smith, 2014]. Thus, under some (rough) flow conditions z_0
110 is a function of both surface and flow properties as indicated by wind-tunnel experiments observing
111 an increase of z_0 with free-stream velocity (or shear velocity) over the same gravel surface where
112 faster aerodynamically rough flows transfer more momentum to the near surface [Dong et al., 2002].
113 In practice, z_0 is at least weakly related to surface properties, and relationships between z_0 and
114 microtopography are exploited frequently to obtain z_0 values.

115

116 With z_0 defined as a property of the air flow, velocity-profile based measurement would seem
117 preferable; however, there are a number of inherent difficulties in adopting this approach. Detailed
118 wind velocity profile measurements over sufficient durations are not always available [e.g. Brock et
119 al., 2006; Rees and Arnold, 2006]. Data requirements are certainly too onerous for distributed
120 measurement of z_0 in this way. Moreover, z_0 values derived from least-squares model fit to velocity
121 measurements are sensitive to instrumental errors [Sicart et al., 2014]. On glaciers, temperature
122 inversions and katabatic winds often result in a wind speed maximum several meters above the
123 surface [e.g. Wallén, 1948; Denby and Greuell, 2000; Giesen et al., 2014; Sicart et al., 2014] and
124 thus deviate from the theoretical profile. Wind velocity profiles need to be adjusted for surface-layer
125 stability and definition of the surface height above which velocity profiles are measured is not
126 straightforward, particularly over rough surfaces [Sullivan and Greeley, 1993; Smeets et al., 1999;
127 Sicart et al., 2014]. Displacement heights are often defined to account for mutual sheltering through
128 addition of a height adjustment to velocity profiles that represents a uniform distribution of the

129 aggregate volume of roughness elements and their wakes [Smith, 2014]. However, there is some
130 uncertainty as to the appropriate level of the zero-reference plane [Munro, 1989; Andreas, 2002].

131

132 Estimations of z_0 from surface microtopography show good agreement with velocity profile derived
133 z_0 values [MacKinnon *et al.*, 2004]. From wind tunnel experiments on sand surfaces, grain-size
134 approaches have been developed [Bagnold, 1941] where z_0 is quantified as $1/30^{\text{th}}$ of a grain diameter.

135 This classic approach is inappropriate for complex ice and snow surfaces that are not composed of
136 individual grains and exhibit multiple scales of topographic variability. An equation developed by
137 Lettau [1969] is used more frequently in studies on ice surfaces, where z_0 is quantified as

138

$$z_0 = 0.5h^* \left(\frac{s}{S} \right) \quad (1)$$

140

141
142 where h^* represents the average vertical extent of microtopographic variations (i.e. effective obstacle
143 height, m), s is the silhouette area facing upwind (i.e. the roughness frontal area, m^2) and S is the unit
144 ground area occupied by each element (i.e. the ‘lot’ area, m^2). The drag coefficient is represented by
145 an ‘average’ drag coefficient of 0.5. The Lettau equation was developed from experiments placing
146 several hundred bushel baskets in a field upwind of an anemometer mast. With such isolated and
147 well-defined roughness elements, specification of each term in (1) is relatively straightforward and
148 results agreed with velocity profile-based z_0 values to $\pm 25\%$. However, on ice surfaces, both velocity
149 profiles and surface roughness are more difficult to measure. Good agreement between eddy
150 covariance, wind velocity profile and microtopographic measurement techniques over ice is often
151 reported (e.g. Brock *et al.*, [2006]), though differences are also apparent. For example, van den Broeke
152 [1996] observed little agreement between the velocity profile and microtopographic methods,
153 calculating a z_0 of 0.8 mm from wind velocity profiles and 120 mm using the Lettau equation (the
154 latter of which was more realistic for the energy balance; Hock, 2005).

155

156 Alternatives to (1) do exist; for example, *Sellers* [1965] estimates z_0 from h^* alone, calibrating a
157 power-law relationship empirically. Meanwhile *Counihan* [1971] and *Fryrear* [1985] use the plan
158 area of roughness elements in place of the frontal area, and *Theurer* [1973] developed an equation
159 that uses both metrics. *Banke and Smith* [1973] and *Andreas* [2011] integrate the Fourier transform
160 of elevations for wavelengths <13 m to relate ice roughness to z_0 . A common simplification of the
161 Lettau equation for complex roughness fields encountered on ice was developed by *Munro* [1989]
162 [section 3.4] and applied to topographic profiles perpendicular to the wind direction. However,
163 sheltering effects from upwind are not taken into account and the ability of single profiles to represent
164 roughness accurately is questionable.

165

166 High resolution topographic data of glacier surfaces are increasingly available [e.g. *Nield et al.*, 2012].
167 From a Digital Elevation Model (DEM) the variability of z_0 for different profiles within the DEM can
168 be reported [*Irvine-Fynn et al.*, 2014]. Yet with advances in surveying techniques and computational
169 power, the advantages of the *Munro* [1989] method in terms of minimal data requirements and
170 computational efficiency have become less relevant. Indeed, estimation of z_0 using profile-based
171 methods results in much of the potentially useful topographic data in three-dimensional point clouds
172 of ice surfaces being discarded and does not make full use of this rich topographic data source
173 [*Passalacqua et al.*, 2015]. It is this shortcoming that we seek to address, through the analysis of
174 multiple point clouds derived from Kårsaglaciären, a small glacier in northern Sweden.

175

176 **3. Methods and Field Site**

177

178 3.1 Field Site

179

180 Kårsaglaciären (68.358739 N, 18.323593 E) is a small ($\sim 1 \text{ km}^2$) mountain glacier located in the
181 Vuottasrita massif, part of the Abisko mountains, on the border between arctic Sweden and Norway.
182 It presently terminates at $\sim 900 \text{ m.asl}$ into a small ice-marginal lake that is developing as the ice
183 margin retreats from a bedrock ridge. Since around 1912 the glacier has been in a state of near
184 constant retreat, but with some isolated areas of minor advance noted [Karlén, 1973; Bodin, 1993].
185 Since the early 1940s the glacier has been included in the Swedish national mass balance programme
186 [Ahlmann and Tryselius, 1926; Wallén, 1948, 1949, 1959; Karlén, 1973; Bodin, 1993]. Climatic
187 conditions at Kårsa are split between maritime (winter) and continental (summer) and dominant winds
188 are katabatic (ice-flow parallel). Wallén [1948, 1949] estimated that turbulent fluxes were responsible
189 for $\sim 40\%$ of ablation at Kårsa.

190

191 3.2 Field data collection

192

193 *3.2.1 Large-Scale DEMs from Terrestrial Laser Scanning*

194 The ablation zone of Kårsaglaciären was surveyed in July 2013 using a RIEGL VZ-1000 terrestrial
195 laser scanner (TLS). While the maximum range of the instrument is stated to be 1400 m [RIEGL,
196 2012], absorbance of the narrow Class 1 infrared laser beam over the wet ice surface reduced the
197 observed maximum range here to $\sim 400 \text{ m}$ on wet ice surfaces. The theoretical data acquisition rate
198 was 100,000 points per second, but again this was reduced with lower point recovery on ice surfaces
199 because of the lower reflectivity of ice at infrared wavelengths. The manufacturer stated precision
200 and accuracy is 0.005 m and 0.008 m respectively [RIEGL, 2012]. A nominal spatial resolution of
201 0.1 m at 450 m range was applied resulting in an angular increment of 0.012° . At large ranges, the
202 laser beam divergence (stated as 0.003 mm m^{-1}) is typically the largest source of error [Carrivick *et*
203 *al.*, 2015] with beam widths of 0.015 m at 500 m range. The relative orientation of the surface would
204 also have influenced the laser beam footprint through determining the angle of incidence.

205

206 Four TLS surveys of Kårsaglaciären were undertaken between 22nd and 24th July 2013 from scan
207 positions surrounding the ~1 km² lower glacier (Figure 1A). There was little overlap between the
208 scans on the glacier ice itself and so gaps in coverage resulted from occlusions behind obstacles or
209 negligible returns from wet ice surfaces oblique to the TLS survey sites (Figure 1B). The first three
210 scan positions were repeated after an interval of three days (25th and 26th July) to yield a second
211 topographic model of the glacier. Accessibility and laser absorbance by snow precluded the
212 acquisition of topographic data from the accumulation zone of the glacier. For survey control, a
213 network of six tripod-mounted static targets was established surrounding the survey area utilising
214 bedrock outcrops and sites clearly visible throughout the survey area (Figure 1A). Using a minimum
215 of four targets visible from each scan position, the TLS surveys were co-registered into a single local
216 co-ordinate system. The standard deviations (or 3D error) of the co-registrations were between 4.5
217 mm and 13.8 mm. The two merged scans of the lower glacier contained 15×10^6 and 9×10^6 points.

218
219 The open-source topographic point cloud analysis toolkit (ToPCAT) [Brasington *et al.*, 2012] was
220 used to unify point densities and create two glacier DEMs. A DEM resolution of 2 m was specified
221 and cells containing fewer than 4 points were discarded (~20% of total cells). The mean cell elevation
222 was applied to represent the glacier surface elevation and the detrended standard deviation of
223 elevations was used to represent sub-grid roughness [Vericat *et al.*, 2014; Smith and Vericat, 2015].
224 The grids of the two DEMs were aligned to enable a DEM of Difference (DoD) to be calculated. The
225 DoD represents changes on the glacier over a three day interval; however, the exact days over which
226 this interval spans are not identical for each scan owing to different days of occupation.

227

228 3.2.2. Plot-scale topography from SfM-MVS

229 To characterize finer scale topographic variability, 31 plots were surveyed using Structure from
230 Motion Multi-View Stereo (SfM-MVS) photogrammetric techniques. The scale-dependence of z_0
231 calculation is an important consideration [Arnold and Rees, 2003; Fassnacht *et al.*, 2009a]. Rees and

232 *Arnold* [2006] observed two scale-free domains (<0.1 m and $>\sim 1$ m), suggesting that the intermediate
233 region is characterized by a definite scale. They suggest that topographic data of sampling interval of
234 <0.1 m and length of >1 m with millimetric vertical accuracy is required to best represent z_0 . Thus,
235 plots were approximately 2 m x 2 m in size and 20 digital photographs of 6 Megapixels were taken
236 of each plot with a Canon PowerShot G11 digital SLR camera. Images surrounding each plot were
237 taken from 2 m above ground with angular changes of $<20^\circ$ between adjacent camera locations to
238 facilitate identification of correct keypoint correspondence [*Moreels and Perona, 2007; Bemis et al.,*
239 *2014*]. Oblique convergent images were captured to avoid the doming effect observed when
240 exclusively vertical images are used [*James and Robson, 2014; Smith and Vericat, 2015*]. Plots were
241 distributed on the glacier surface to incorporate the greatest possible range of surface type and
242 topographic variability and to ensure, as far as possible, good spatial coverage of the lower glacier
243 surface (Figure 1A). Glacier surface types were classified into qualitative categories including
244 smooth/superimposed ice, runnels, cryoconite, sun cups, blocky crystalline ice, supraglacial channels,
245 dirty ice, light/medium/dense scree, shallow/deep crevasses and snow (Table S1).

246

247 Groups of photographs pertaining to each plot were imported into Agisoft Photoscan Professional
248 1.1.6, and SfM algorithms implemented, to estimate simultaneously camera positions, camera
249 intrinsic parameters and scene geometry (see *James and Robson* [2012] and *Smith et al.* [2015] for
250 further details). Georeferencing of the SfM point cloud was performed using control points surveyed
251 with a TLS. Five reflective disk targets (50 mm diameter) were fixed into the ice in the plot corners
252 and plot centre and directed to face the nearest TLS scan position. The targets were identified in
253 additional TLS surveys undertaken from each scan position that were focused on each plot. The 3D
254 co-ordinates of each target (referenced to the same local co-ordinate system as the TLS surveys) were
255 imported, and a linear similarity transformation performed to scale and georeference each SfM point
256 cloud. Average georeferencing errors were sub-cm (see Supplementary Information Table S1). Using
257 these coordinates the intrinsic camera parameters and scene geometry were refined and the bundle

258 adjustment re-run to optimize the image alignment by minimising the sum of the reprojection error
259 and the georeferencing error. Both original and optimized point clouds were calculated and MVS
260 image matching algorithms performed to produce final dense point clouds (Figure 1C). Average point
261 density of the final plot point clouds was $>300,000$ points m^{-2} . ToPCAT was applied to the plot-scale
262 SfM-MVS surveys for the generation of a DEM of 5 mm resolution. While TLS surveys of each plot
263 were performed as part of the georeferencing, the absorbance of the near-infrared laser by ice and
264 snow was such that relatively few TLS points were observed within each plot (typically 500 points
265 m^{-2}) but this was sufficient to validate the SfM-MVS point clouds.

266

267 To analyze the temporal variability of ice surface roughness, of the 31 plots, 9 were revisited after 3
268 days (Plots A–C, E, F, H and S–V; Figure 1A). TLS targets were replaced and re-surveyed as
269 described above. Additionally, 3 of these 9 plots (A, B and F) were re-surveyed again a few hours
270 afterwards.

271

272 To facilitate upscaling, the extent of each plot was mapped onto the glacier-scale TLS-derived DEM.
273 Plot extents and DEM cells did not align perfectly owing to the variability of plot spacing, so the
274 mean sub-grid roughness value of all cells containing at least part of each plot was calculated to
275 compare plot-scale and glacier-scale models. The DEM surveyed on the same day as the plot was
276 used in each case.

277

278 *3.2.3. Meteorological data*

279 Meteorological data were recorded during the survey interval to explain the surface lowering rates
280 observed. Air temperature was monitored every 30 minutes throughout the field campaign at an
281 automatic weather station (AWS) located ~ 500 m down-valley of the glacier terminus. The AWS
282 comprised a Campbell Scientific CR200 data logger connected to an air pressure, air temperature,

283 relative humidity, wind speed and wind direction sensors. This AWS has been in operation since 2007
284 and mean July temperatures have been 8.6°C, compared to -10.6°C in February.

285

286 3.3 Validation of SfM-MVS surveys

287

288 TLS data co-incident and contemporaneous with each SfM-MVS plot survey were used to validate
289 both non-optimized and optimized SfM-MVS dense point clouds. Cloud-to-cloud comparisons were
290 conducted in CloudCompare (CloudCompare 2.6.1, 2016). The 3D distance between each TLS point
291 and its nearest neighbour in the dense SfM-MVS cloud was computed and split into X, Y and Z
292 components. Where either the X or Y components were >0.02 m, the validation point was discarded.
293 The mean and median Z distances were calculated alongside the standard deviation and RMSE of the
294 errors for each plot. Beam divergence and laser footprint long axis were calculated (after *Schürch et*
295 *al.*, [2011]) to estimate the error of the TLS validation data. While only negligible differences between
296 RMSE values for optimized and non-optimized SfM-MVS point clouds were observed (typically ~ 1
297 mm), for each plot the point cloud with the lowest RMSE was used for analysis.

298

299 3.4 z_0 calculation

300

301 Each plot-scale point cloud was rotated to be aligned with the prevailing wind direction, observed to
302 be predominantly down-glacier. Point clouds were cropped to ensure an approximately equal number
303 of rows and columns. We undertook three different approaches, described in sequence below, to
304 estimate z_0 from the microtopographic roughness data acquired. The first follows the method of
305 *Munro* [1989] for the purposes of comparison with previous studies; the remaining two present new
306 methods which utilize the greater volume of roughness information that can be gathered using raw
307 and gridded TLS and SfM-MVS data sets. Differences between the three methods are summarized in
308 Table 1.

309

310 3.4.1 Profile-based approach

311 To estimate z_0 following *Munro* [1989], we simplify the Lettau equation (1) by assuming that h^* can
312 be represented by twice the standard deviation of elevations of the detrended profile ($2\sigma_d$, m), with
313 the mean elevation set to zero (Figure 2A) (similar to the ‘random roughness’ metric commonly
314 applied to soil and snow surfaces [e.g. *Kuipers*, 1957; *Fassnacht et al.*, 2009a]). Roughness elements
315 are modeled by calculating the number of upcrossings above the mean elevation (f) in any profile of
316 length X (m). The frontal silhouette area of roughness elements in the profile is then estimated as

317

$$318 \quad s = \frac{2\sigma_d X}{2f}$$

319 (2)

320 and the ground area occupied by each roughness element (so-called ‘lot’ area), S (m²), is
321 approximated as

322

$$323 \quad S = \left(\frac{X}{f}\right)^2.$$

324 (3)

325 Thus the aerodynamic roughness length for a given profile becomes

326

$$327 \quad z_0 = \frac{f}{X} (\sigma_d)^2.$$

328 (4)

329 As demonstrated in Figure 2A, (4) makes the assumption of uniformly distributed roughness elements
330 of equal height along the profile. Despite this, *Munro* [1989] found that it performed well as an
331 approximation of z_0 differing by only 12% from the true z_0 value (though note the later re-analysis of
332 *Andreas* [2002] which questioned height corrections to velocity profiles implemented by *Munro*
333 [1989]). Using this method, z_0 was calculated for every profile ($n \approx 400$) in both orthogonal directions

334 for each plot. Since profiles should be taken perpendicular to the wind direction, to avoid confusion,
335 we state consistently wind direction when describing the z_0 value. Following normality tests, the
336 probability distribution of profile-based z_0 values was characterized by the mean and standard
337 deviation of values in each orthogonal direction.

338

339 3.4.2. DEM-based approach

340 Profile-based simplifications, while computationally efficient, discard large volumes of potentially
341 useful topographic data. Such simplifications are more appropriate for the situation faced by *Munro*
342 [1989] where, prior to the widespread application of TLS or SfM-MVS, limited manually measured
343 point data were available (~30 points) and more demanding z_0 calculation methods cannot be
344 supported. With a DEM-based approach, the following assumptions of the profile approach can be
345 relaxed:

346 [1] All roughness elements are of equal height.

347 [2] All roughness elements are equally spaced.

348 [3] No sheltering of roughness elements occurs.

349 [4] The frontal area of roughness elements is equal for opposing wind directions (isotropy).

350

351 Considering the *Lettau* [1969] equation, a DEM-based approach enables the roughness frontal area s
352 to be calculated directly (Figure 2B) for each cardinal wind direction, thereby relaxing assumptions
353 [1], [2] and [4]. Sheltering (assumption [3]) is implicitly represented by including only frontal areas
354 above the detrended zero plane. Calculating the combined roughness frontal area across the plot, the
355 planar plot area is then used as the ground area S (since the ‘lot’ area per roughness element as
356 specified by *Lettau* [1969] incorporates both the ground area of the roughness element and the
357 surrounding plot area). Specifying the effective obstacle height h^* is more problematic, and the
358 rationale for the use of $2\sigma_d$ by *Munro* [1989] is unclear. Considering assumption [3], only points that
359 are above the detrended plane are considered and h^* is instead calculated as the mean deviation above

360 this plane. Any single summary of obstacle height will be somewhat arbitrary; however, the mean
361 deviation above this plane is perhaps most meaningful on an irregular ice surface. This DEM-based
362 approach results in four z_0 values are generated for each plot, one for each cardinal direction.

363

364 3.4.3. Point cloud-based approach

365 High resolution surveying techniques produce dense point clouds containing rich information that
366 require summary even for DEM construction. Using several simplifying assumptions, the dense point
367 clouds were employed here directly, for a further method of z_0 calculation as follows.

368

369 Raw point clouds are not of a uniform density as the feature matching process as part of the SfM-
370 MVS workflow may oversample more visible local topographic highs owing to their greater visibility
371 in the raw images and higher density of successful matches [Smith *et al.*, 2015]. To yield a uniform
372 point density the plot-scale point clouds were subsampled after detrending using an octree filter (a
373 tree-based method of point cloud partitioning) [Meagher, 1982]. Normal vectors for each point were
374 computed using triangulation (Figure 2C) and the number of normal vectors facing each cardinal
375 direction (i.e. within a 90° bin centred on the cardinal direction) was counted to represent s in each
376 cardinal direction under the assumption that each point represents a comparable surface area
377 following octree subsampling. Points below the detrended plane and ‘flat’ surfaces defined as having
378 a normal vector greater than 80° from horizontal were not used in the estimation of s . The plot area S
379 was approximated by the total number of points in the cloud (approximating the 3d surface area).
380 Finally, the effective obstacle height was calculated as the mean height above the detrended plane of
381 all points above that plane.

382

383 4. Results

384

385 4.1 Validation of SfM-MVS

386

387 Quantitative comparison of SfM-MVS points with TLS survey points demonstrated good agreement
388 between the two datasets. In 4 plots TLS surveys showed insufficient points for comparison with
389 SfM-MVS owing to the poor reflectance of wet ice at the instrument wavelength. Across the
390 remaining 27 plots for which validation data were available, the average Mean Absolute Error (MAE)
391 for non-optimized point cloudes was 8.47 mm. Optimized SfM-MVS models performed slightly
392 better (8.14 mm), though there was little observable difference between them (full details in Tables
393 S1 and S2). However, MAE values were an order of magnitude below the mean of the estimated
394 maximum error in the TLS points (69.66 mm) owing to the sometimes long survey ranges and beam
395 divergence. Restricting analysis to situations where modeled TLS error was <10 mm, non-optimized
396 and optimized MAE values were 6.02 and 5.55 mm respectively. Given the much shorter survey
397 range for SfM-MVS than TLS, it is reasonable to assume that expected errors are lower from plot-
398 scale SfM-MVS than for glacier-scale TLS and are mm-scale (see *Smith and Vericat*, [2015]).

399

400 4.2 Spatial variability in ice z_0

401

402 4.2.1. *Comparison of z_0 calculations*

403

404 Table 2 shows the results for z_0 calculation from the three different methods. Using the concordance
405 correlation [*Lin*, 1989, 2000] which measures agreement of variables rather than linearity, we found
406 that when averaged in all directions the strongest agreement was between DEM-based and point-
407 cloud-based z_0 calculations ($\rho_c = 0.973$), with lower agreement between profile-based z_0 values and
408 both DEM-based (0.730) and cloud-based (0.620) values. Separating the values into orthogonal
409 components showed weaker agreement but a similar pattern (Figure S1). In general, point-cloud-
410 based z_0 values were the highest (and had the lowest inter-quartile range) and DEM-based values the

411 lowest, though differences between all three calculation methods were relatively minor with a range
412 in overall average z_0 values of just 0.247 mm (Table 2).

413

414 4.2.2. *Variability of z_0 between plots*

415

416 A wide range of z_0 values was observed across the 31 plots on the ablation zone of Kårsaglaciären
417 (Figure 3A). Summary statistics are separated out by direction in Table 2 and values for each plot are
418 provided in Table S3. All z_0 values were > 0.05 mm and the majority were < 3 mm. All plots
419 containing deep crevasses and one containing shallow crevasses yielded values > 10 mm, comparable
420 with those reported on very rough glacier ice [Smeets *et al.*, 1999]. Plots traversed by supraglacial
421 channels exhibited consistently high z_0 values (> 1 mm), while plots containing dirt cones on the ice
422 surface also yielded locally high values. The presence of scree distributed over the ice surface also
423 produces a high z_0 (~ 1 mm); however, the extent of debris cover is important with lower areal
424 concentrations exhibiting a lower z_0 (particularly for the DEM-based approach). The lowest z_0 values
425 were for surfaces classified as ‘smooth’, ‘slushy’ or ‘superimposed’ ice (< 0.3 mm). Intermediate
426 values were observed for patches of snow cover, sun cups, runnels and patches classified as ‘dirty
427 ice’ (with z_0 typically between 0.5 and 1 mm).

428

429 4.2.3. *Variability of profile values within a plot*

430

431 DEM and cloud-based methods generate a single value for the plot (for each cardinal direction),
432 whereas extraction of profile-based z_0 values from a DEM enables multiple values to be compared
433 for a single plot. Skewness-kurtosis tests confirmed normality of all sets of profiles; only one plot
434 was not normal at $P < 0.01$ and all plots were normal at $P < 0.05$. With over 400 profile-based z_0
435 measurements in each direction per plot, analysis of the standard deviation of these values is
436 informative (Figure 3B; Figure S2). Mean values are consistently in line with DEM-based and cloud-

437 based values; however, the variability about that mean is substantial. For two plots, the standard
438 deviation of z_0 is greater than the mean. In all cases the high standard deviation of >20% of the mean
439 z_0 value presents an important sampling issue for conventional topographic profiles.

440

441 4.2.4. Anisotropy

442

443 In Table 2, the largest differences between z_0 calculation methods emerge when the directionality of
444 surface roughness is considered. Following *Smith et al.* [2006], an anisotropy ratio (Ω) is calculated
445 for comparison of surface roughness in wind parallel ($z_{0\parallel}$) and wind-perpendicular ($z_{0\perp}$) directions.

446

447

$$\Omega = \frac{z_{0\parallel} - z_{0\perp}}{z_{0\parallel} + z_{0\perp}}$$

448

(5)

449

450 This ratio tends towards 1 when $z_{0\parallel}$ dominates, towards -1 when $z_{0\perp}$ dominates, and 0 when roughness
451 is isotropic. Setting the down-glacier direction as parallel to the prevailing wind, Figure 4 summarizes
452 the variation of anisotropy values between z_0 calculations. Profile-based metrics indicate greater z_0
453 for glacier-flow parallel winds and exhibit the largest range, DEM-based metrics suggest generally
454 isotropic surfaces and have the smallest range of values, whereas cloud-based metrics highlight
455 greater z_0 for winds blowing across the glacier. Detection of anisotropy thus appears to be an
456 important discriminant of the metrics examined here.

457

458 A breakdown by plot is provided in Table S3 and Figure S3. The most extreme anisotropy ratio values
459 (and the biggest differences between metrics) are observed in plots containing large surface features,
460 such as crevasses or supraglacial channels. The specific values are sensitive to the orientation of the
461 channel within the plot. However, no significant relationship was observed between anisotropy and
462 z_0 . The presence of debris often resulted in positive anisotropy ratios.

463

464 While profile-based approaches only separate orthogonal components, DEM-based analyses
465 produced a z_0 value for each cardinal direction and point-cloud-based metrics can yield a z_0 value for
466 any given wind direction, though here, for comparability, only values for cardinal directions have
467 been calculated. The difference between z_0 for two opposing wind directions is summarized as a
468 percentage of the average z_0 value (for both directions). The DEM-based z_0 values exhibit greater
469 variability for opposing wind directions (32% and 22% for glacier flow parallel and perpendicular
470 components respectively) than cloud-based z_0 values (9% and 12% respectively).

471

472 4.3 Modeling surface roughness at the glacier scale

473

474 Statistical relationships were explored between plot-scale z_0 and glacier-scale variables to provide a
475 basis for upscaling z_0 beyond the plot (Figure 5A-C). Large values of z_0 associated with crevasses had
476 a significant leverage over such statistical relationships. Thus, the four plots that comprise Figure
477 3Aii were excluded from upscaling analysis [*Hessel and Hirsch, 1982*]. A further plot, located in the
478 accumulation area was excluded as there were insufficient co-incident TLS data.

479

480 No statistically significant relationships were observed between z_0 and plot mean elevation, plot
481 distance from glacier terminus or plot mean slope. However, a significant relationship was observed
482 between sub-grid TLS roughness and all three z_0 values; the relationship was strongest for DEM-
483 based z_0 values (Figure 5B). This relationship presented the possibility of upscaling z_0 estimates
484 beyond the plot to represent z_0 variability over the majority of the lower glacier (where data are
485 available), though since differences in absolute z_0 values between methods were smaller than the
486 natural variability of z_0 on a single glacier, all three calculation methods are likely to be equally
487 suitable in this regard. The relationship for DEM-based z_0 values was used to provide such a glacier

488 scale z_0 map in Figure 5D using the first TLS survey as a basis for upscaling. As plot data were only
489 reliable where $z_0 < 3$ mm, only cells in this range were included.

490

491 Across the glacier, areas of relatively high z_0 values were found to be associated with crevasse features
492 (Figure 5D) and the medial moraine running through the centre of the glacier. Considering only the
493 0.14 km² area of the ablation area of Kårsaglaciären for which sufficient TLS data were available to
494 estimate z_0 , the mean modeled z_0 was 0.99 mm, the median value was 0.85 mm and the standard
495 deviation was 0.61 mm. This is likely to be an underestimate of z_0 as some notable areas of high sub-
496 grid roughness were not able to be included (e.g. close to the glacier terminus).

497

498 4.4 Temporal changes in z_0

499

500 *4.4.1 Glacier-scale changes*

501

502 Over the 3 day TLS survey interval, a substantial amount of ice surface lowering was observed
503 throughout the ablation zone (Figure 6A). To demonstrate that the observed lowering is not a survey
504 artefact, the change detected in two bedrock areas was compared with that seen on the ice surface
505 (Figure 6B and C). The two distributions are statistically different. Median change observed by TLS
506 over bedrock was 7.28 mm (over 7,532 m² outlined in bold in Figure 6A), whereas that observed on
507 ice surfaces was -206.99 mm (over 0.12 km²). At higher elevations within the survey area, surface
508 lowering rates (~150 mm) are slightly less than at the glacier margins and across the lower parts of
509 the glacier (~200 mm). Relatively high rates of lowering (~280 mm) were observed on the true right
510 of the glacier which corresponds to the entry point of a stream running under the ice along the glacier
511 margin, fed by a waterfall indicated in the lower left of Figure 6A. A large area at the true left margin
512 of the glacier close to the south-facing bedrock outcrop also showed higher than average lowering
513 (~250–300 mm). Large elevation changes (> 2 m) were also observed at the terminus where

514 Kårsaglaciären calves into a small proglacial lake. Glacier advances and calving events can be clearly
515 observed from the DoD at the terminus (Figure 6A) and represent the biggest elevation changes over
516 the three day survey interval.

517

518 *4.4.2. Plot-scale changes*

519

520 The change in z_0 observed over the 9 resurveyed plots is summarized in Figure 7. Plots were
521 resurveyed after an interval of 0.5, 3 and/or 3.5 days resulting in a maximum of four time periods for
522 a single plot. Values for all three z_0 calculation metrics are presented, incorporating averaged values
523 for all directions and values separated into both down-glacier and across-glacier averages. Analysis
524 of the AWS record revealed that the period following 23rd July 2013 (Figure 6E) was considerably
525 warmer than any time previously in the melt season of 2013 when average daily temperatures rarely
526 rose above 10°C.

527

528 Despite high rates of surface lowering (e.g. Figure 6D), estimated z_0 values (Figure 7) remained
529 relatively constant for three plots containing surface meltwater features (supraglacial channels or
530 runnels). Decreases in z_0 were observed for plots where surface debris was observed (dirty ice or
531 debris band) or which contained minor stress features (a shallow crevasse or crevasse traces), while
532 increases in z_0 were observed where the ice was very smooth and on a plot pocked with cryoconite.
533 All three z_0 values were well correlated and, as reported in section 4.2.1, point-cloud-based z_0 values
534 were typically highest while profile-based z_0 values had the highest variability.

535

536 Over three days, observed surface lowering was typically ~0.2 m; however, three plots exhibited
537 much higher values >0.45 m. These rapidly lowering plots covered a wide range of z_0 values,
538 including the more deeply incised of the two supraglacial channels and crevasse traces and smooth
539 ice, all of which were located in the upper ablation zone towards the true left margin of the glacier.

540 Overall, observed surface lowering was positively correlated with degree days ($r = 0.87$, $n = 24$, $P <$
541 0.0001). The three rapidly lowering plots experienced surface lowering rates between 10.2 and 11.1
542 $\text{mm K}^{-1} \text{day}^{-1}$ while other plots were between 4.2 and $7.0 \text{ mm K}^{-1} \text{day}^{-1}$.

543

544 **5. Discussion**

545

546 5.1 Methods for calculating z_0 from topographic data

547

548 Previously, collection of topographic data suitable for z_0 calculation required either laborious and
549 time-consuming measurement or the construction of bespoke equipment [e.g. *Herzfeld et al.*, 2000].

550 Recent advances in the acquisition of high resolution topography have revolutionized the study of
551 Earth-surface processes [*Passalacqua et al.*, 2015], yet the calculation of z_0 from ice surface
552 topography has typically retained assumptions put in place under conditions of limited topographic
553 data and computational power. With these restrictions lifted, the DEM-based analysis presented
554 herein permits frontal area exposed to a prevailing wind direction to be calculated explicitly over an
555 ice (or snow) surface. Furthermore, with alternative approximations, z_0 can be rapidly estimated
556 directly from point clouds.

557

558 Overall differences between profile, raster and cloud-based z_0 measurements were relatively minor
559 (Table 2). More detailed comparison of calculation methods reveals three weaknesses in the
560 conventional topographic profile-based approach. First, calculating z_0 from a single topographic
561 profile presents a sampling issue given the variability of topographic profile-based values within a
562 single plot (Figure 3B). Similar z_0 variability was also reported by *Irvine-Fynn et al.* [2014]. Second,
563 while orthogonal profiles are often computed, the different frontal areas from two opposing wind
564 directions cannot be resolved. DEM-based z_0 values for opposing wind directions differed by $> 20\%$
565 meaning conventional approaches may not be appropriate for anisotropic surfaces. Third, topographic

566 profile-based z_0 values do not account for sheltering of an obstacle. With many ice-surface features
567 streamlined either by wind or water flows having continuous topographic expressions for 10s of
568 meters or more (sastrugi, for example; *Jackson and Carroll* [1978]), such an assumption is limiting
569 for glacier surfaces. This important weakness is revealed when z_0 values are separated into orthogonal
570 directions (Figure 4).

571

572 In the extreme case where a crevasse or supraglacial channel is aligned perpendicular to the prevailing
573 wind direction (Figure 8A) a detrended topographic profile will not detect this feature even if located
574 within the crevasse or channel and would yield a relatively low z_0 value. Conversely, if the plot were
575 rotated by 90° (Figure 8B) a detrended topographic profile perpendicular to the wind direction would
576 yield a relatively high z_0 value. However, visual examination of the two plot surfaces in Figure 8
577 reveals that the plot in Figure 8A has a greater frontal area exposed to the prevailing wind, whereas
578 the plot in Figure 8B is relatively streamlined to the wind direction. In this case computing z_0 using
579 frontal area calculated from a DEM or approximated from a point cloud results in a higher z_0 for Plot
580 8A; the opposite of profile-based z_0 values. Such differences are not seen when uniform arrays of
581 discrete roughness elements are present (from which the *Lettau* [1969] equation was derived) and are
582 only significant where natural streamlined surfaces are the focus of study.

583

584 5.2 Spatial variability of z_0 and potential for upscaling

585

586 A wide range of z_0 values for ice surfaces is reported in the literature; yet in this study a similar range
587 of z_0 values was observed over a single glacier ablation area. Our mean z_0 value of ~ 1 mm reflects
588 the typical values reported in the literature [*Brock et al.*, 2006]. Indeed the ‘typical’ ice roughness
589 value of 0.66 mm that is applied in the glacier-scale distributed surface energy balance model of
590 *Arnold et al.* [2006] is similar to our median modeled value of 0.85 mm (Figure 5D). However,
591 considering DEM-based z_0 values in this study, variation over three orders of magnitude was detected

592 from 0.05 mm on superimposed ice to 22 mm for a deep crevasse. It is clear that a single z_0 value
593 cannot accurately represent the important contribution of z_0 to glacier melt. Prominent surface features
594 (e.g. crevasses) result in locally high z_0 values. Scale-dependency of z_0 values requires further
595 investigation; however, the sampling method used here captures the length scales identified by *Rees*
596 *and Arnold* [2006].

597

598 The significance of the relationship between z_0 calculated from plot-scale SfM-MVS and glacier-
599 scale TLS roughness suggests that the relevant components of topographic variability influencing z_0
600 can be approximated at the glacier scale. The modeled z_0 map presented in Figure 5D contains
601 substantial data gaps, though these could be filled with a dense network of survey stations. However,
602 caution is required since approximation of z_0 with a simple metric of sub-grid roughness is a
603 considerable simplification and does not capture the directional variability observed with the more
604 sophisticated metrics we investigated at the plot scale. Nevertheless, the relationships in Figure 5
605 suggest that a reasonable approximation of glacier-scale z_0 variability can be made using topographic
606 data products that are increasingly available. Indeed, with the increased ease of data acquisition,
607 upscaling z_0 to represent the variability over the glacier-scale becomes a distinct possibility. Existing
608 large scale TLS [e.g. *Kerr et al.*, 2009; *Nield et al.*, 2012] and SfM-MVS [e.g. *Immerzeel et al.*, 2014;
609 *Ryan et al.*, 2015] survey campaigns demonstrate this enhanced capability clearly.

610

611 Glacier surface energy balance calculations require estimates of turbulent fluxes of sensible and latent
612 heat and these are typically derived from high-resolution meteorological observations alongside a
613 single z_0 value to represent the ice surface [e.g. *Arnold et al.*, 2006]. However, as this study has shown,
614 an assumption of homogeneous z_0 values over entire glacier surfaces is questionable. Derivation of a
615 distributed z_0 map such as is presented in Figure 5D therefore opens up several key possibilities for
616 those interested in modeling glacier surface energy balance. First, it allows the modeller to compare
617 z_0 acquired at a point with a range of values across a whole glacier and thus assess how representative

618 it is. Second, it permits analyses of scale dependence. Since velocity-profile measurements of z_0
619 reflect not just the surface in the immediate vicinity of the velocity profile, but are the aggregate effect
620 of surface obstacles distributed over a larger fetch area, a z_0 value for a single 4 m² cell in Figure 5D
621 cannot be directly compared with velocity profile derived z_0 values at that same point. Rather,
622 aggregation of heterogeneous z_0 values over areas representing an estimated fetch of the wind enables
623 comparison with wind-profile derived values [Panofsky, 1984]. The distributed nature of z_0 in Figure
624 5D will also assist with future calculations of varying z_0 values with varying wind direction. Finally,
625 given that many inputs to surface energy balance models are gridded datasets, the inclusion of a
626 dynamic and distributed z_0 map, rather than a single assumed value, is a logical next step.

627

628 5.3. Temporal variability of z_0

629

630 Our observations of temporal variability in ice surface roughness with surface melt were acquired on
631 Kårsaglaciären during a short period of relatively high air temperatures and agree with previously
632 reported findings [e.g. Brock *et al.*, 2000, 2006; Smeets and van den Broeke, 2008]. Ice with surface
633 debris or small amounts of dirt on the surface tended to become smoother, as did surfaces exhibiting
634 small crevasse features suggesting preferential melting out of protruding roughness. Supraglacial
635 channels did not exhibit such a decline in roughness possibly as down-cutting kept pace with
636 preferential melting. This variable response contrasts with the systematic increase in roughness
637 observed on melting snow surfaces [Fassnacht *et al.*, 2009b].

638

639 Substantial surface melt was recorded over just 4 days (Figures 6 and 7). Average surface lowering
640 was 0.2 m and showed a similar association between surface lowering rates and degree days as
641 reported for Norwegian glaciers by Laumann and Reeh [1993] (5.5-7.5 mm K⁻¹ day⁻¹) and rates are
642 similar to the maximum values reported in Wallén [1948]. Three plots showed substantially higher
643 surface lowering rates; these could not be discriminated by surface roughness or other features and

644 instead appeared to reflect variation in incoming radiation being relatively flat plots positioned close
645 to a south-facing slope. Although surface lowering rates were rapid, the monitoring interval of just 4
646 days is insufficient to quantify the full range of ice roughness variability through the melt season.
647 With a longer monitoring period over seasonal timescales, a wider range of roughness values is likely
648 to be observed.

649

650 5.4. Further work

651

652 The alternative z_0 calculation methods introduced here require validation using velocity-profile or
653 eddy-correlation data [Nield *et al.*, 2013]. Similarly, modeled z_0 variability at the glacier scale requires
654 validation both through finer scale measurements and through incorporation into spatially distributed
655 surface energy balance models that are in turn validated against proglacial stream discharge
656 measurements. Velocity profile data are needed alongside the distributed z_0 map of Figure 5D and
657 map of glacier surface change in Figure 6A to validate the novel approach of z_0 estimation outlined
658 herein and to examine the relevant scales at which to aggregate microtopography-derived z_0 estimates.
659 With glacier-scale topography acquired through TLS or SfM-MVS, distributed energy balance
660 models have the potential to incorporate sophisticated models of insolation by calculating shading
661 from valley topography directly. Orthophotograph mosaics are a further output of plot-scale SfM-
662 MVS that could be used to estimate surface albedo directly [Dumont *et al.*, 2011; Rippin *et al.*, 2015].
663 In addition, glacier-scale surveys may be able to bridge the gap between microtopography and
664 satellite remote sensing of glacier surfaces for a more extensive upscaling of z_0 as demonstrated by
665 *Blumberg and Greeley* [1993] and investigated on glacier surfaces by *Rees and Arnold* [2006].

666

667 Conventional methods of estimating z_0 from topographic profiles make several assumptions about the
668 nature of the surface which is typically simplified as a regular array of uniform roughness elements
669 (e.g. Figure 2A). Here we have presented a novel method of calculating z_0 directly from high

670 resolution DEMs that does not rely upon such simplifying assumptions. However, further
671 investigation as to the specific parameters used in z_0 calculation (detailed in Table 1) is required,
672 particularly the representation of effective obstacle height.

673

674 Sheltering of surfaces has been studied in detail in the atmospheric sciences and in investigations of
675 aeolian erosion [e.g. *Garratt, 1992; Bottema, 1996; Chappell and Heritage, 2007*]. While *Garratt*
676 [1992] suggested a displacement height of $0.7h^*$ for most natural surfaces, the assumption made in
677 Table 1 (for DEM-based and cloud-based z_0 calculations) was that frontal areas below the detrended
678 plane level would be effectively sheltered. For the ice surfaces investigated herein, roughness element
679 density (i.e. frontal area divided by surface area; *Wooding et al., 1973*) was <0.13 in all plots aside
680 from one deeply crevassed plot and thus still within the range for which the *Lettau* [1969] equation
681 holds. Certainly more sophisticated sheltering parameterisations should be investigated [see *Raupach,*
682 *1992; Chappell et al., 2010*] and the availability of high resolution topographic data facilitates more
683 direct inclusion of mutual sheltering of roughness elements [see *Smith, 2014*]. Similarly, the average
684 drag coefficient of 0.5 used here is likely to be an overestimate for many glacier surfaces which tend
685 to be streamlined [*Wieringa, 1993; Smeets et al., 1999*] in at least one direction and would thus exhibit
686 a much lower drag coefficient [*Powell, 2014*]. As demonstrated in Figure 8, the degree of streamlining
687 and hence the drag coefficient may be dependent on the wind direction.

688

689 **6. Conclusions**

690

691 Through direct representation of the surface area of roughness elements more sophisticated
692 parameterisations of z_0 from ice surface topography can be realized from high-resolution three-
693 dimensional survey data. Properties of surface roughness that best represent the process of momentum
694 transfer from air flows to the ice surface can be quantified directly, enabling calculation of z_0 from
695 topographic data to better reflect the underlying theoretical equations. When averaged over all

696 cardinal wind directions, there is little difference between the novel DEM-based z_0 values and values
697 calculated from profiles using assumptions on the form of surface roughness. However, large
698 differences emerge when z_0 is calculated separately for each wind direction, particularly where
699 surface roughness is anisotropic.

700

701 The aerodynamic roughness of ice surfaces can be estimated at the glacier scale using a relationship
702 established between z_0 and sub-grid roughness of topographic models gridding at the meter-scale.
703 Such upscaling is important considering: (i) the wide variability of z_0 over three orders of magnitude
704 over a relatively small glacier ablation zone; (ii) the lack of a statistical relationship between z_0 and
705 more general topographic variables such as elevation and slope; and (iii) the relatively large effect
706 that z_0 variability has on estimations of turbulent heat fluxes and glacier ice melt, particularly in the
707 context of future climate warming. With increased availability of high resolution topographic data at
708 the glacier scale, surface energy balance models can incorporate distributed z_0 parameterisations and
709 better predict rates of ice loss under climate change scenarios.

710

711 **Acknowledgements**

712 Fieldwork was funded by EU INTERACT grants awarded to Bingham (LARGE) and Rippin
713 (SAGLA) and a grant from the Carnegie Trust for the Universities of Scotland awarded to Bingham.
714 We gratefully thank the Abisko Scientific Research Station (ANS) for hospitality and logistical
715 support and Kallax Flyg for helicopter support.

716

717 **References**

718

719 Ahlmann, H. W., and O. Tryselius (1929), Der Kårsa-Gletscher in Schwedisch-Lappland, *Geogr.*
720 *Ann.*, 11, 1–32.

721

722 Andreas, E. L. (2002), Parameterizing scalar transfer over snow and ice: a review, *J.*
723 *Hydrometeorology*, 3(4), 417–432.

724

725 Andreas, E. L. (2011), A relationship between the aerodynamic and physical roughness of winter sea
726 ice, *Q. J. R. Meteorol. Soc.*, 137, 1581–1588.

727

728 Arnold, N. S., and W. G. Rees (2003), Self-similarity in glacier surface characteristics, *J. Glaciol.*,
729 49(167), 547–554.

730

731 Arnold, N. S., W. G. Rees, A. J. Hodson, and J. Kohler (2006), Topographic controls on the surface
732 energy balance of a high Arctic valley glacier, *J. Geophys. Res.*, 111, F02011,
733 doi:10.1029/2005JF000426.

734

735 Bagnold, R. A. (1941), *The Physics of Wind-blown Sand and Desert Dunes*, 265(10), Methuen,
736 London.

737

738 Banke, E.G., and S. D. Smith, (1973), Wind stress on Arctic sea ice, *J. Geophys. Res.*, 78, 7871–
739 7883.

740

741 Bemis, S. P., S. Micklethwaite, D. Turner, M. R. James, S. Akciz, S. T. Thiele, and H. A. Bangash
742 (2014), Ground-based and UAV-Based photogrammetry: A multi-scale, high-resolution mapping
743 tool for structural geology and paleoseismology, *J. Structural Geology*, 69, 163–178.

744

745 Bintanja, R. and M. R. van den Broeke (1994), Local climate, circulation and surface-energy balance
746 of an Antarctic blue-ice area, *Ann. Glaciol.*, 20, 160–168.

747

748 Bintanja, R. and M. R. van den Broeke (1995), The surface energy balance of Antarctic snow and
749 blue ice, *J. Appl. Meteorol.*, 34(4), 902–926.

750

751 Blumberg, D. G., and R. Greeley (1993), Field studies of aerodynamic roughness length, *J. Arid*
752 *Environments*, 25 39–48.

753

754 Bodin, A. (1993), Physical properties of the Kårsa glacier, Swedish Lapland, Stockholm, University
755 of Stockholm, Department of Physical Geography, Research Report 17.

756

757 Bottema, M., (1996), Roughness parameters over regular rough surfaces: experimental requirements
758 and model validation. *J. Wind Eng. Ind. Aerodyn.*, 64, 249–265.

759

760 Braithwaite, R. J. and O. B. Olesen (1990), Response of the energy balance on the margin of the
761 Greenland ice sheet to temperature changes, *J. Glaciol.*, 36, 217–21.

762

763 Brasington, J., D. Vericat, and I. Rychkov (2012), Modelling river bed morphology, roughness and
764 surface sedimentology using high resolution terrestrial laser scanning, *Water Resour. Res.* 48,
765 W11519, doi:10.1029/2012WR012223.

766

767 Brock, B. W., I. C. Willis, M. J. Sharp, and N. S. Arnold (2000), Modelling seasonal and spatial
768 variations in the surface energy balance of Haut Glacier d’Arolla, Switzerland, *Ann. Glaciol.*, 31, 53–
769 62.

770

771 Brock, B. W., I. C. Willis and M. J. Sharp (2006), Measurement and parameterization of aerodynamic
772 roughness length variations at Haut Glacier d’Arolla, Switzerland, *J. Glaciol.*, 52, 281–297.

773

774 Brock, B. W., C. Mihalcea, M. P. Kirkbride, G. Diolaiuti, M. E. J. Cutler, and C. Smiraglia (2010),
775 Meteorology and surface energy fluxes in the 2005–2007 ablation seasons at the Miage debris-
776 covered glacier, Mont Blanc Massif, Italian Alps, *J. Geophys. Res.*, 115, D09106,
777 doi:10.1029/2009JD013224.

778

779 Carrivick, J. L., M. W. Smith, and D. M. Carrivick (2015), High-resolution topography of the upper
780 Tarfala valley, *GFF*, 1–14.

781

782 Chappell, A., and G. L. Heritage (2007), Using illumination and shadow to model aerodynamic
783 resistance and flow separation: an isotropic study, *Atmospheric Environment*, 41, 5817–5830.

784

785 Chappell, A., S. Van Pelt, T. Zobeck, and Z. Dong (2010), Estimating aerodynamic resistance of
786 rough surfaces using angular reflectance, *Remote Sensing of Environment*, 114, 1462–1470.

787

788 CloudCompare (2016), CloudCompare version 2.6.1, GPL software. Retrieved from
789 <http://www.cloudcompare.org/>

790

791 Counihan, J. (1971), Wind tunnel determination of the roughness length as a function of the fetch and
792 the roughness density of three-dimensional roughness elements, *Atmospheric Environment*, 5, 637–
793 642.

794

795 Denby, B., and W. Greuell (2000), The use of bulk and profile methods for determining surface heat
796 fluxes in the presence of glacier winds, *J. Glaciol.*, 46(154), 445–452.

797

798 Denby, B. and P. Smeets (2000), Derivation of turbulent flux profiles and roughness lengths from
799 katabatic flow dynamics, *J. Appl. Meteorol.*, 39(9), 1601–1612.

800

801 Dong, Z., X. Lui, and X. Wang (2002), Aerodynamic roughness of gravel surfaces, *Geomorphology*,
802 43, 17–31.

803

804 Dumont, M., P. Sirguey, Y. Arnaud, and D. Six (2011), Monitoring spatial and temporal variations
805 of surface albedo on Saint Sorlin Glacier (French Alps) using terrestrial photography, *Cryosphere*,
806 5(3), 759–771.

807

808 Fassnacht, S. R., J. D. Stednick, J. S. Deems, and M. V. Corrao (2009a), Metrics for assessing snow
809 surface roughness from digital imagery, *Water Resour. Res.*, 45, W00D31,
810 doi:10.1029/2008WR006986.

811

812 Fassnacht, S. R., M. W. Williams, and M. V. Corrao (2009b), Changes in the surface roughness of
813 snow from millimetre to metre scales." *Ecological Complexity*, 6, 221–229.

814

815 Fryrear, D. W. (1985), Soil cover and wind erosion, *Trans. ASAE*, 28, 781–784.

816

817 Garratt, J. R. (1992), *The Atmospheric Boundary Layer*, 336 pp., Cambridge atmospheric and space
818 science series, Cambridge University Press, Cambridge, U. K.

819

820 Giesen, R. H., L. M. Andreassen, J. Oerlemans, and M. R. Van Den Broeke (2014), Surface energy
821 balance in the ablation zone of Langfjordjøkelen, an arctic, maritime glacier in northern Norway, *J.*
822 *Glaciol.*, 60(219), 57–70.

823

824 Greuell, W., and C. Genthon (2004), Modelling land-ice surface mass balance. *Mass Balance of the*
825 *Cryosphere: Observations and Modelling of Contemporary and Future Changes*, 117–168.

826

827 Greuell, W., and P. Smeets (2001), Variations with elevation in the surface energy balance on the
828 Pasterze (Austria), *J. Geophys. Res.*, 106(D23), 31717–31727.

829

830 Hay, J. E., and B. B. Fitzharris (1988), The synoptic climatology of ablation on a New Zealand
831 glacier, *J. Climatology*, 8, 201–215.

832

833 Helsel, D. R., and R. M. Hirsch (1992), *Statistical Methods in Water Resources*, Springer-Verlag,
834 New York.

835

836 Herzfeld, U. C., H. Mayer, W. Feller, and M. Mimler (2000), Geostatistical analysis of glacier-
837 roughness data, *Ann. Glaciol.*, 30, 235–242.

838

839 Hock, R. (2005), Glacier melt: a review of processes and their modelling, *Progress in Physical*
840 *Geography*, 29(3), 362-391.

841

842 Hock, R., and B. Holmgren (1996), Some aspects of energy balance and ablation of Storglaciären,
843 northern Sweden, *Geogr. Ann.*, 78A(2–3), 121–131.

844

845 Hock, R., and B. Holmgren (2005), A distributed surface energy-balance model for complex
846 topography and its application to Storglaciären, Sweden, *Journal of Glaciology*, 51(172), 25–36.

847

848 Holmgren, B. (1971), *Climate and energy exchange on a sub-polar ice cap in summer. Arctic Institute*
849 *of North America Devon Island Expedition 1961-1963*, Uppsala, Meteorologiska Institutionen,
850 Uppsala Universitet, Meddelande 107, Part A-E.

851

852 Immerzeel W. W., P. D. A. Kraaijenbrink, J. M. Shea, A. B. Shrestha, F. Pellicciotti, M. F. P.
853 Bierkens, and S. M. de Jong (2014), High-resolution monitoring of Himalayan glacier dynamics using
854 unmanned aerial vehicles, *Remote Sensing of Environment*, 150, 93–103.

855

856 Irvine-Fynn, T. D. L., E. Sanz-Ablanedo, N. Rutter, M. W. Smith, and J. H. Chandler (2014),
857 Measuring glacier surface roughness using plot-scale, close-range digital photogrammetry, *J.*
858 *Glaciol.*, 60, 957–969.

859

860 Ishikawa, N., I. F. Owens, and A. P. Sturman (1992), Heat balance characteristics during fine periods
861 on the lower parts of the Franz Josef Glacier, South Westland, New Zealand, *Int. J. of Climatology*,
862 12(4), 397–410.

863

864 Jackson, B. S., and J. J. Carroll (1978), Aerodynamic roughness as a function of wind direction over
865 asymmetric surface elements, *Bound.-Lay. Meteorol.*, 14, 323–330.

866

867 James, M. R., and S. Robson (2012), Straightforward reconstruction of 3D surfaces and topography
868 with a camera: accuracy and geoscience application, *J. Geophys. Res.: Earth Surface* 117, F03017,
869 doi: 10.1029/2011JF002289.

870

871 James, M. R., and S. Robson (2014), Mitigating systematic error in topographic models derived from
872 UAV and ground-based image networks, *Earth Surf. Processes Landforms*, 39, 1413–1420, doi:
873 10.1002/esp.3609.

874

875 Karlén, W. (1973), Holocene glacier and climatic variations, Kebnekaise Mountains, Swedish
876 Lapland, *Geogr. Ann.*, 55A(1), 29–63.

877

878 Kerr, T., I. Owens, W. Rack, and R. Gardner (2009), Using ground-based laser scanning to monitor
879 surface change on the Rolleston Glacier, New Zealand, *J. Hydrol.*, 48, 59–71.
880

881 Kuipers, H. (1957), A reliefmeter for soil cultivation studies, *Neth. J. Agric. Sci.*, 5, 255–267.
882

883 Laumann, T., and N. Reeh (1993), Sensitivity to climate change of the mass balance of glaciers in
884 southern Norway, *J. Glaciol.*, 39, 656–665.
885

886 Lettau, H. H. (1969), Note on aerodynamic roughness parameter estimation on the basis of roughness
887 element description, *J. Applied Meteorology*, 8, 828–832.
888

889 Lin, L. I.-K. (1989), A concordance correlation coefficient to evaluate reproducibility, *Biometrics*,
890 45, 255–268.
891

892 Lin, L. I. -K. (2000), A note on the concordance correlation coefficient, *Biometrics*, 56, 324–325.
893

894 MacKinnon, D. J., G. D. Clow, R. K. Tigges, R. L. Reynolds, and P. S. Chavez (2004), Comparison
895 of aerodynamically and model-derived roughness lengths (z_0) over diverse surfaces, central Mojave
896 Desert, California, USA, *Geomorphology*, 63(1), 103–113.
897

898 Marcus, M. G., R. D. Moore, and I. F. Owens (1984), Short-term estimates of surface energy transfers
899 and ablation on the lower Franz Josef Glacier, South Westland New Zealand, *New Zealand J. Geology
900 and Geophys.*, 28, 559–67.
901

902 Meagher, D. (1982), Geometric modelling using octree encoding, *Computer Graphics and Image
903 Processing*, 19, 129–147.

904

905 Millikan, C. M. (1938), A critical discussion of turbulent flows in channels and circular tubes,
906 *Proceedings of the 5th International Congress on Applied Mechanics Cambridge, MA*, 386–392.

907

908 Moreels, P., and P. Perona (2007), Evaluation of features detectors and descriptors based on 3d
909 objects, *Int. J. Comp. Vis.*, 73(3), 263–284.

910

911 Müller, F., and C. M. Keeler (1969), Errors in short-term ablation measurements on melting ice
912 surfaces, *J. Glaciol.*, 8(52), 91–105.

913

914 Munro, D. S. (1989), Surface roughness and bulk heat transfer on a glacier: comparison with eddy
915 correlation, *J. Glaciol.*, 35(121), 343–348.

916

917 Nield, J. M., R. C. Chiverrell, S. E. Darby, J. Leyland, L. H. Vircavs, and B. Jacobs (2012), Complex
918 spatial feedbacks of tephra redistribution, ice melt and surface roughness modulate ablation on tephra
919 covered glaciers, *Earth Surf. Processes Landforms*, 38(1), 95–102.

920

921 Nield, J. M., J. King, G. F. Wiggs, J. Leyland, R. G. Bryant, R. C. Chiverrell, S. E. Darby, F. D.
922 Eckardt, D. S. G. Thomas, L. H. Vircavs, and R. Washington (2013), Estimating aerodynamic
923 roughness over complex surface terrain, *J. Geophys. Res.: Atmospheres*, 118(23), 12–948.

924

925 Panofsky, H. A. (1984), Vertical variation of the roughness length at the boulder atmospheric
926 observatory, *Bound.-Lay. Meteorol.*, 28, 305–308.

927

928 Passalacqua, P., P. Belmont, D. M. Staley, J. D. Simley, J. R. Arrowsmith, C. A. Bode, C. Crosby, S.
929 B. DeLong, N. F. Glenn, S. A. Kelly, D. Lague, H. Sangireddy, K. Schaffrath, D. G. Tarboton, T.

930 Wasklewicz, and J. M. Wheaton (2015), Analyzing high resolution topography for advancing the
931 understanding of mass and energy transfer through landscapes: A review, *Earth-Science*
932 *Reviews*, 148, 174–193.

933

934 Powell, D. M. (2014), Flow resistance in gravel-bed rivers: Progress in research, *Earth-Science*
935 *Reviews*, 136, 301–338.

936

937 Prandtl, L. (1926), Über die ausgebildete Turbulenz, *Proceedings of the 2nd International Congress*
938 *of Applied Mechanics Zürich*, 62–74.

939

940 Raupach, M.R., (1992), Drag and drag partition on rough surfaces, *Bound.-Layer Meteorol.*, 60, 375–
941 395.

942

943 Rees, W. G. and N. S. Arnold (2006), Scale-dependent roughness of a glacier surface: implications
944 for radar backscatter and aerodynamic roughness modelling, *J. Glaciol.*, 52, 214–222.

945

946 RIEGL (2012), Data Sheet Riegl VZ-1000.

947 http://www.riegl.com/uploads/tx_pxpriegldownloads/DataSheet_VZ-1000_2015-03-24.pdf (Date
948 Accessed 21st August 2015).

949

950 Rippin, D. M., A. Pomfret, and N. King (2015), High resolution mapping of supraglacial drainage
951 pathways reveals link between micro-channel drainage density, surface roughness and surface
952 reflectance, *Earth Surf. Processes Landforms*, doi: 10.1002/esp.3719.

953

954 Ryan J. C., A. L. Hubbard, J. E. Box, J. Todd, P. Christoffersen, J. R. Carr, T. O. Holt and N. Snooke
955 (2015), UAV photogrammetry and structure from motion to assess calving dynamics at Store Glacier,
956 a large outlet draining the Greenland ice sheet, *The Cryosphere*, 9(1), 1–11.

957

958 Schürch, P., A. L. Densmore, N. J. Rosser, M. Lim, and B. W. McArdell (2011) Detection of surface
959 change in complex topography using terrestrial laser scanning: application to the Illgraben debris-
960 flow channel, *Earth Surf. Processes Landforms* 36(14), 1847–1859.

961

962 Sellers, W. (1965), *Physical Climatology*, 272 pp., University of Chicago Press, Chicago.

963

964 Sicart, J. E., M. Litt, W. Helgason, V. B. Tahar, and T. Chaperon (2014), A study of the atmospheric
965 surface layer and roughness lengths on the high-altitude tropical Zongo glacier, Bolivia, *J. Geophys.*
966 *Res. Atmos.*, 119, 3793–3808, doi:10.1002/2013JD020615.

967

968 Smeets, C. J. P. P., and M. R. van den Broeke (2008), Temporal and spatial variations of the
969 aerodynamic roughness length in the ablation zone of the Greenland ice sheet, *Bound.-Lay.*
970 *Meteorol.*, 128(3), 315–338.

971

972 Smeets, C. J. P. P., P. G. Duynkerke and H. F. Vugts (1999), Observed wind profiles and turbulence
973 fluxes over an ice surface with changing surface roughness, *Bound.-Lay. Meteorol.*, 92(1), 101–123.

974

975 Smith, B. E., C. F. Raymond, and T. Scambos (2006), Anisotropic texture of ice sheets, *J. Geophys.*
976 *Res.*, 111, F01019, doi:10.1029/2005JF000393.

977

978 Smith, M. W. (2014), Roughness in the Earth Sciences, *Earth-Science Reviews*, 136, 202–225. doi:
979 10.1016/j.earscirev.2014.05.016.

980

981 Smith, M. W., and D. Vericat (2015), From experimental plots to experimental landscapes:
982 topography, erosion and deposition in sub-humid badlands from Structure-from-Motion. *Earth Surf.*
983 *Processes Landforms*, 40, 1656–1671.

984

985 Smith, M. W., J. L. Carrivick, and D. J. Quincey (2015), Structure from motion photogrammetry in
986 physical geography, *Progress in Physical Geography*, doi: 10.1177/0309133315615805.

987

988 Sullivan, R., and R. Greeley (1993), Comparison of aerodynamic roughness measured in a field
989 experiment and in a wind tunnel simulation, *Journal of Wind Engineering and Industrial*
990 *Aerodynamics*, 48(1), 25–50.

991

992 Theurer, W. (1973), Dispersion of ground-level emissions in complex built-up areas, Ph.D. Thesis,
993 University of Karlsruhe, Germany (in German).

994

995 van den Broeke, M. (1996), Characteristics of the lower ablation zone of the west Greenland ice sheet
996 for energy-balance modelling, *Ann. Glaciol.*, 23, 160–66.

997

998 Vericat, D., M. W. Smith, and J. Brasington (2014), Patterns of topographic change in sub-humid
999 badlands determined by high resolution multi-temporal topographic surveys, *Catena*, 120, 164–176.

1000

1001 Wallén, C. C. (1948), Glacial–meteorological investigations on the Karsa Glacier in Swedish
1002 Lapland, *Geogr. Ann.*, 30(3–4), 451–672.

1003

1004 Wallén, C. C. (1949), Shrinkage of the Karsa Glacier and its probable meteorological causes, *Geogr.*
1005 *Ann.*, 31(1–2), 275–291.

1006

1007 Wallén, C. C. (1959), The Karsa Glacier and its relation to the climate of the Torne Trask region,
1008 *Geogr. Ann.*, 41(4), 236–244.

1009

1010 Wieringa, J. (1993), Representative roughness parameters for homogeneous terrain, *Bound.-Lay.*
1011 *Meteorol.*, 63, 323–363.

1012

1013 Wooding, R. A., E. F. Bradley, and J. K. Marshall, (1973), Drag due to regular arrays of roughness
1014 elements of varying geometry, *Bound.-Layer Meteorol.*, 5, 285–308.

1015

1016 **Tables**

1017

Table 1. Summary of z_0 calculations.

1018

Quantity	Profile-based	DEM-based	Cloud-based
Drag coefficient		0.5	
Effective obstacle height h^* (m)	$2 \times$ detrended standard deviation of profile perpendicular to wind	Mean height of all points above the detrended plane	
Ground area S (m ²)	For each ‘roughness element’ separately: $(X/f)^2$.	Full plot planar area	Full plot 3d surface area approximated by number of points after octree subsampling. No units.
Silhouette area s (m ²)	Uniform roughness elements approximated. Frontal area of a ‘typical’ roughness element calculated using equation 2 (see Figure 2A).	Exposed frontal area for each cardinal direction calculated across whole DEM. Only includes areas above detrended plane.	Surface area facing each cardinal direction estimated by counting number of points with normal vector 45° either side of that direction. Only points above detrended plane where normal vector is $<80^\circ$ from horizontal. No units.

1019

1020 **Table 2.** Summary of z_0 values for all 31 plots. The wind direction is given (i.e. wind blowing from
1021 ‘up-glacier’ or from the ‘true left’, etc.). Thus, ‘glacier flow parallel’ profile-based values are for
1022 profiles orientated across the glacier surface (i.e. perpendicular to the wind direction). Robust

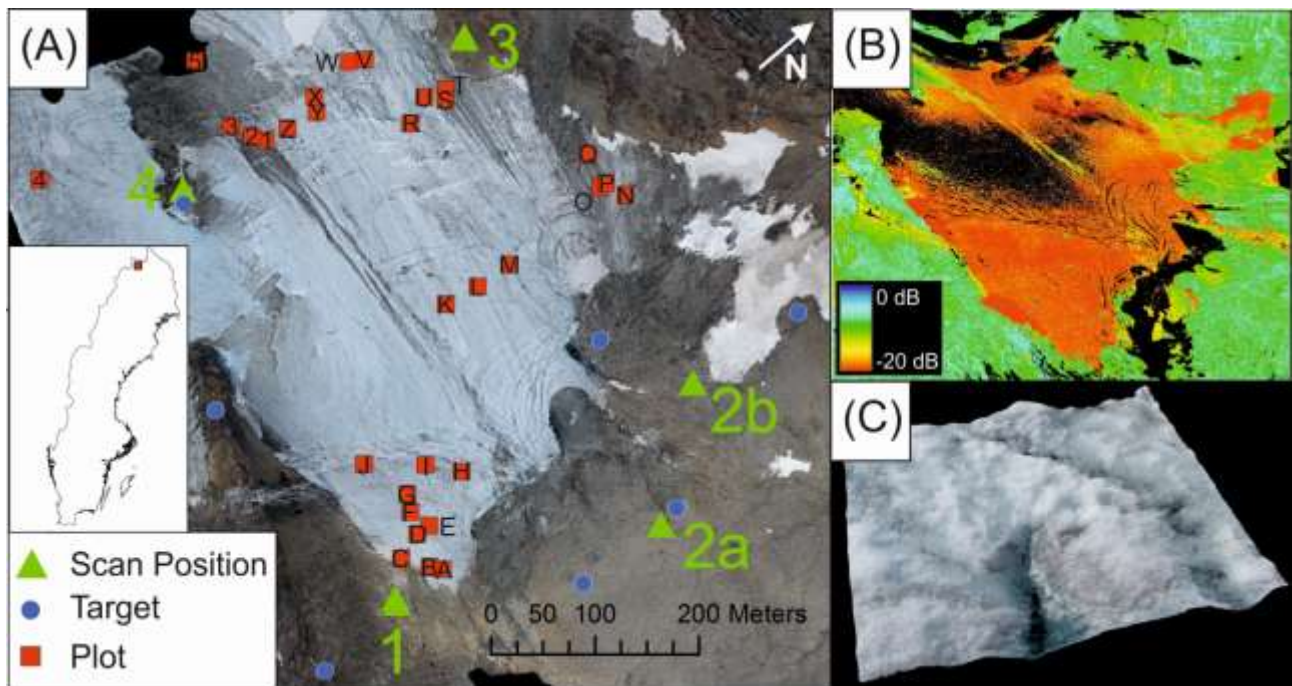
1023 metrics provided owing to the non-normality of the dataset (see outliers on the right panel of Figure
 1024 2A). IQR = Inter Quartile Range.

Z ₀ method	Direction (wind)						Overall average
	Up-glacier	Down-glacier	Glacier flow parallel average	True-Left	True-Right	Glacier flow perpendicular average	
Profile							
Median (mm)			1.216			0.760	1.019
IQR (mm)			1.044			1.778	1.340
DEM							
Median (mm)	0.741	1.026	0.883	0.772	0.843	0.757	0.820
IQR (mm)	0.953	1.015	1.392	0.980	0.938	0.877	1.110
Point Cloud							
Median (mm)	1.071	0.941	0.998	1.227	1.222	1.269	1.067
IQR (mm)	1.160	0.883	1.009	0.977	1.081	1.029	0.947

1025

1026

1027 **Figures**



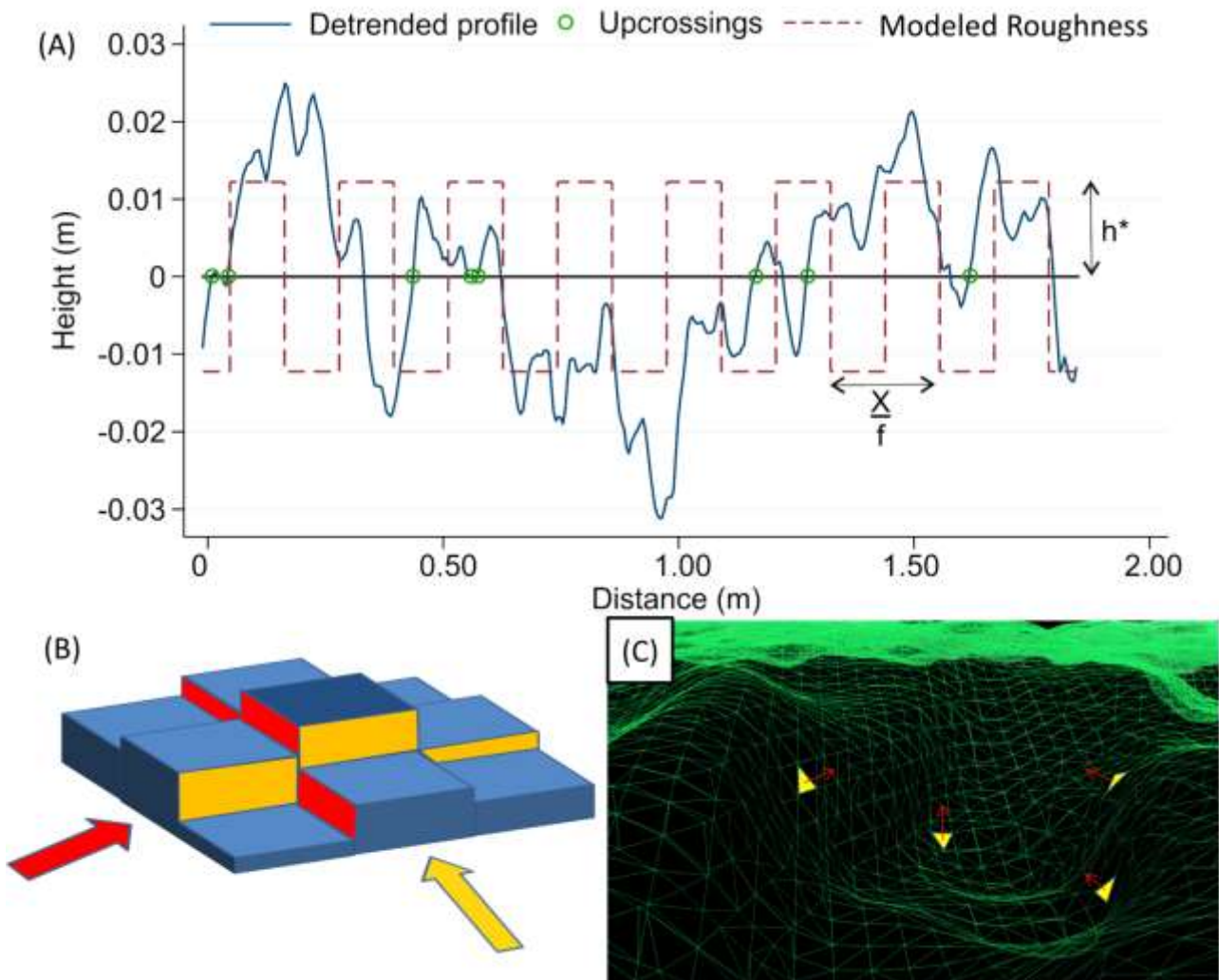
1028

1029

1030 **Figure 1.** Study site. (A) Scan positions, targets and plot locations overlaid onto an
 1031 orthophotograph of lower Kårsaglaciären generated from glacier-scale SfM-MVS (not
 1032 contemporaneous with plot surveys and used to generate an orthophotograph only). See Table S1

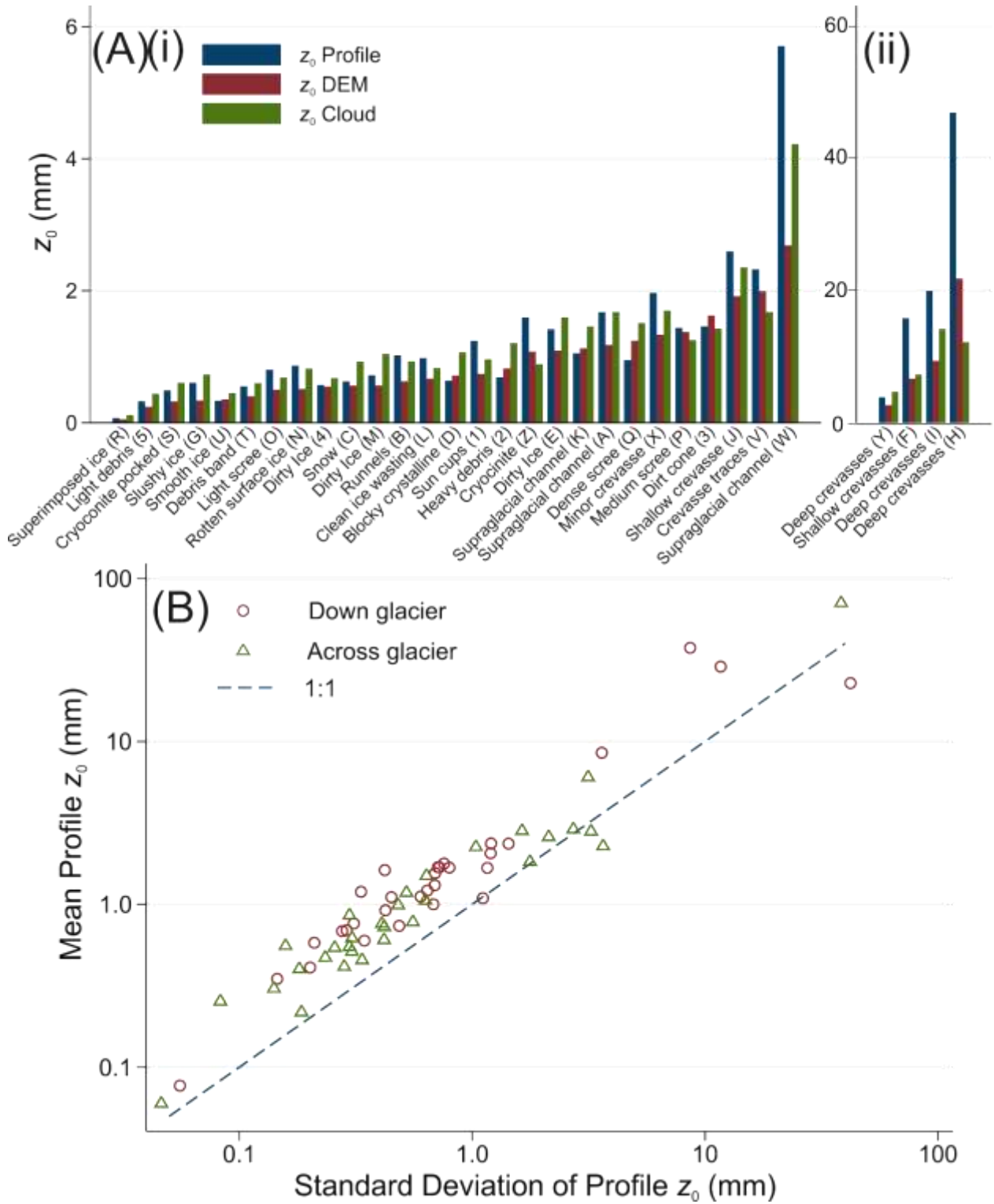
1033 for plot descriptions. Note the location of Scan 2 varied slightly between the two surveys; (B)
 1034 oblique viewpoint of TLS point cloud of the lower Kårsaglaciären rendered by return reflectance
 1035 (dB) displaying areas of wet ice oblique to the TLS that exhibited low point density (in black); (C)
 1036 example SfM-MVS plot dense point cloud viewed obliquely (Plot A, supraglacial channels, approx.
 1037 2 x 2 m).

1038



1039

1040 **Figure 2.** Schematic illustrations of z_0 calculations. (A) Conventional profile-based approach
 1041 (shown for Plot N). Upcrossings are defined as points where the profile crosses the detrended mean
 1042 moving from below the mean to above the mean. (B) DEM-based approach highlighting frontal
 1043 area for two orthogonal wind directions. (C) demonstration of normal vectors on a triangulated
 1044 wireframe mesh of a point cloud (Plot N, for illustration only).



1046

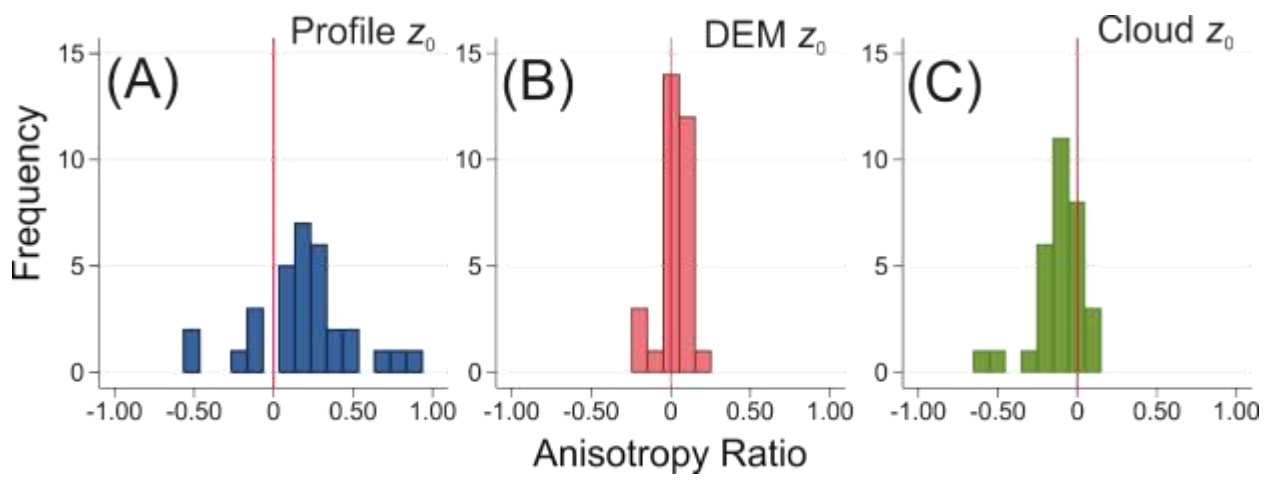
1047 **Figure 3.** (A) Variability of z_0 between plot surfaces (ordered by z_0 DEM). See Table S3 for values.

1048 Plot IDs provided in parentheses (see Figure 1A for locations). Directionally averaged z_0 values are

1049 presented for each plot. (B) Relationship between mean and standard deviation of profile-based z_0

1050 values presented separately for each orthogonal direction. Note log-log scale.

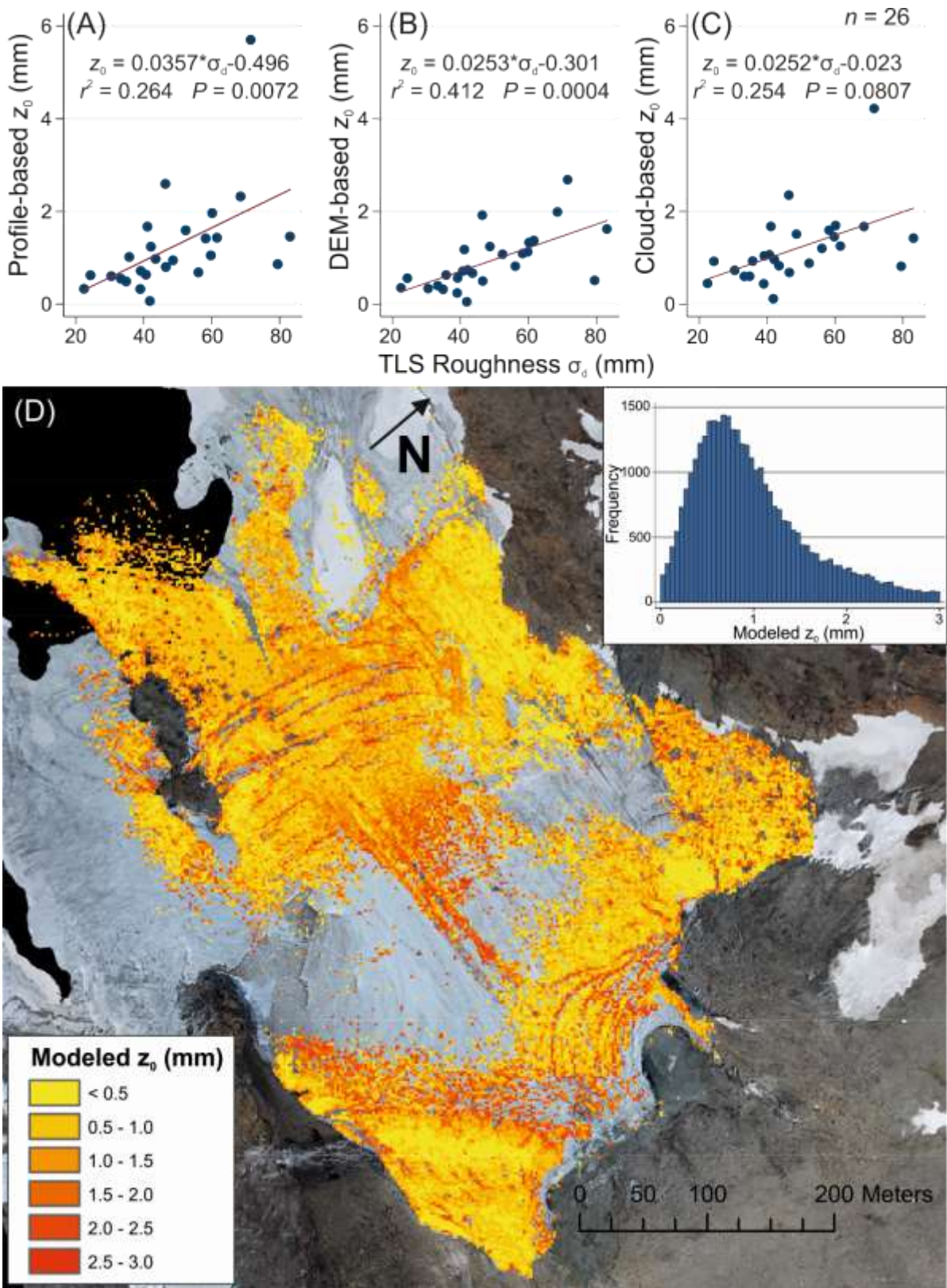
1051



1052

1053

Figure 4. Summary of anisotropy ratio values for each method of z_0 calculation.



1054

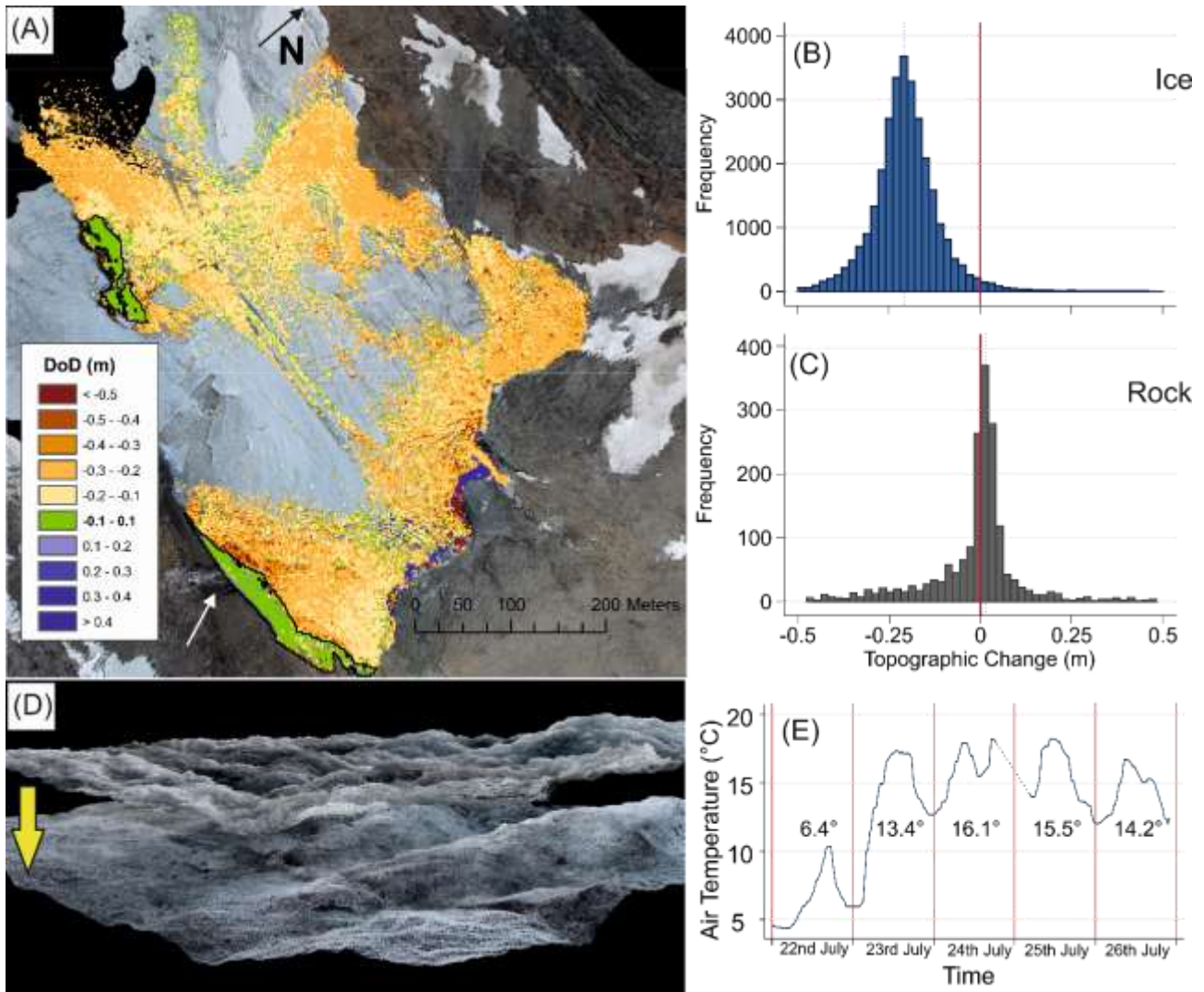
1055 **Figure 5** (A-C) Relationships between directionally averaged z_0 values and sub-grid TLS roughness

1056 (represented by the detrended standard deviation of elevations). Model fits correspond to the

1057 regression parameters indicated (excludes Plots F, H, I and Y). (D) Map of modeled glacier z_0 using

1058 TLS-derived sub-grid roughness to upscale DEM-based z_0 (2 m resolution). Gaps relate to areas

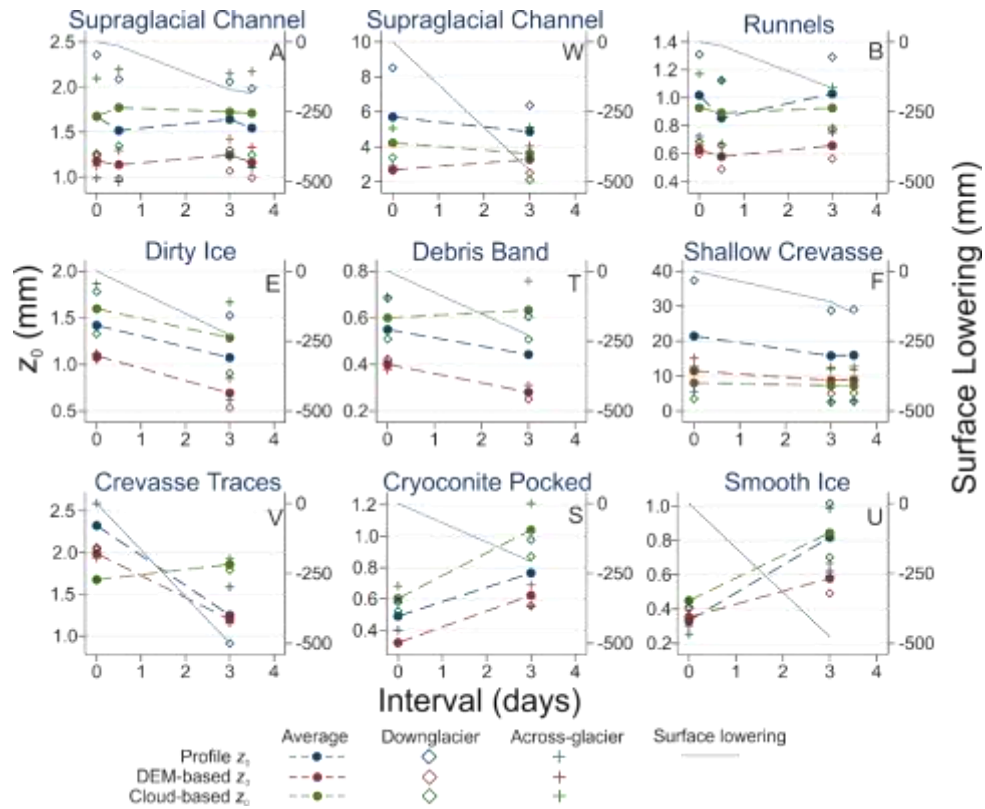
1059 with insufficient TLS data to compute sub-grid roughness or areas where predicted z_0 is > 3 mm and
 1060 beyond the range of the relationship demonstrated in Figure 5B. The distribution of modeled z_0
 1061 values is shown (inset).
 1062



1063
 1064 **Figure 6.** (A) DEM of Difference from repeat TLS over a three day interval. Bedrock areas are
 1065 outlined in black. The waterfall supplying a subglacial stream is indicated with a white arrow. (B)
 1066 Frequency histogram of observed topographic changes for ice surfaces and (C) for rock and
 1067 proglacial debris surfaces. Only changes ± 0.5 m shown for clarity. (D) Example of lowering
 1068 observed from repeat SfM-MVS dense point clouds ('Dirt Ice' Plot E over a 3 day interval showing
 1069 an average surface elevation change of 0.23 m); (E) 30-minute smoothed temperature data recorded

1070 at the AWS over the survey interval. Mean daily temperatures reported for each day. A data gap
 1071 spanning 24th and 25th July has been interpolated (dashed line).

1072

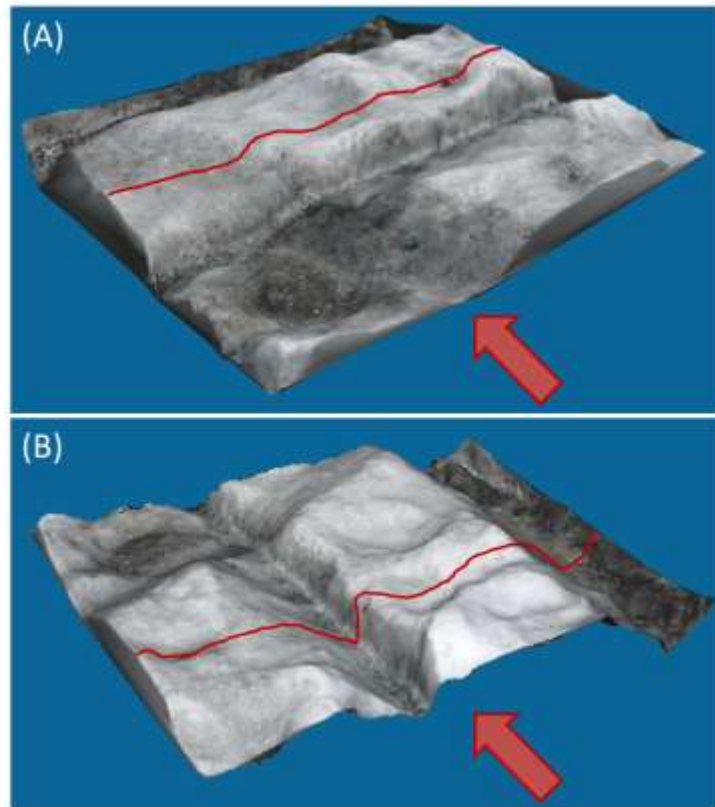


1073

1074

1075 **Figure 7.** Plot-scale changes in z_0 values with surface lowering over several days of intense melting
 1076 (Figure 6E). Note different scales on z_0 axes for improved clarity of changes within each plot. Plot
 1077 IDs are indicated in the top-right corner of each panel and relate to Figure 1A. Survey intervals
 1078 were not exactly contemporaneous with the DoD in Figure 6A.

1079



1080

1081

1082

1083

1084

1085

1086

Figure 8. Demonstration of differences between z_0 anisotropy ratios for different calculation methods. The plot surface in (A) is rotated through 90 degrees in (B), while the prevailing wind direction remains constant. A greater frontal area is exposed to the prevailing wind in (A); however a profile perpendicular to the wind direction shows greater topographic variability in (B).